UNIVERSITEIT VAN PRETORIA
UNIVERSITY OF PRETORIA
YUNIBESITHI YA PRETORIA

THE EFFECT OF PARTICLE SHAPE ON SOLID ENTRAINMENT IN GAS–SOLID FLUIDISATION

Wouter de Vos

UNIVERSITEIT VAN PRETORIA
UNIVERSITY OF PRETORIA
YUNIBESITHI YA PRETORIA

The Effect of Particle Shape on Solid Entrainment in Gas–Solid Fluidisation

by

Wouter de Vos

A thesis submitted in fulfillment
of the requirements for the subject CVD 800

Masters of Engineering (Chemical Engineering)

in the

Chemical Engineering
Faculty of Engineering, the Built Environment and Information Technology

University of Pretoria
Pretoria

26th February 2008

The Effect of Particle Shape on Solid Entrainment in Gas–Solid Fluidisation

Author:	Wouter de Vos
Supervisor:	E.L. Du Toit
Co-supervisor:	W. Nicol
Department:	Department of Chemical Engineering University of Pretoria
Degree:	Master of Engineering (Chemical Engineering)

Synopsis

The entrainment rate of Ferrosilicone (FeSi) particles was measured in a 140 mm perspex column with air as the fluidising medium. Two different types of FeSi were used, namely atomised FeSi, which is mostly spherical in shape with smooth surfaces, and milled FeSi, which is irregular with rough surfaces. Both the FeSi mixtures had the same solid density and the similar average particle diameters ranging from 38 μm to 50 μm. The size and density of these particles put them on the border between Geldart A and Geldart B powders, similar to the high temperature Fischer-Tropsch catalyst. The atomised FeSi had a slightly higher concentration in fines (8.6% vs 1.8%), but except for the difference in particle shape, the two mixtures had otherwise very similar physical properties.

A substantial difference in entrainment rate was measured between the atomised and milled FeSi, where the atomised had an entrainment rate of about six times higher than the milled FeSi throughout the range of superficial velocities tested. It was shown that the higher entrainment rate cannot be attributed only to the higher fines concentration, but that the difference in particle shape had a significant effect on the entrainment rate.

Several two dimensional shape characterisation techniques were used in attempt to quantify the difference between the atomised and the milled FeSi. Of these the particle circularity managed to differentiate the best between the two particle mixtures. The circularities of the atomised and the milled FeSi were found to be 0.782 and 0.711 respectively.

The measured circularity was used instead of a sphericity to adjust for the effect of particle shape on the terminal velocity of the particles. The adjusted terminal velocity was then used in the elutriation rate constant correlations to see which of the popular correlations in literature predicts the entrainment rate of the FeSi the best. All of the correlations gave a poor performance in predicting the measured entrainment rates. The two correlations that performed the best were that of Choi et al. (1999) (AARE = 72.6%) and Geldart et al. (1979) (AARE = 79%).

It was concluded that single particle drag and single particle terminal velocities are not adequate to incorporate the effect of particle shape on entrainment rate. The method by which shape affects entrainment rate therefore deserves further investigation. Further studies should also be done to develop a three dimensional shape descriptor that predicts bulk behaviour better.

KEYWORDS: gas–solid fluidisation, entrainment, particle shape, particle shape description, fischer-tropsch

CONTENTS

1 Introduction **1**

2 Literature Study **3**

2.1 Fluidisation 3
  2.1.1 Solid classification 4
  2.1.2 Fluidisation regimes 5
  2.1.3 Zones in a fluidised bed 8
2.2 Entrainment 9
  2.2.1 Particle transport into freeboard 9
  2.2.2 Flow structure in freeboard 10
2.3 Factors influencing entrainment and elutriation 11
  2.3.1 Effect of reactor properties 11
  2.3.2 Effect of fluid properties 13
  2.3.3 Effect of particle properties 17
2.4 Modelling Entrainment and Elutriation 25
  2.4.1 Entrainment flux 25
  2.4.2 Elutriation rate constant 26
2.5 Concluding remarks 32

3 Experimental **34**

3.1 Experimental Setup 34
  3.1.1 Materials 34
  3.1.2 Equipment 35
3.2 Method 36
  3.2.1 Minimum fluidisation measurements 37
  3.2.2 Entrainment measurements 37

3.2.3 Repeatability 38
3.2.4 Procedure verification 39
3.3 Image Processing 42

4 Results and discussion **45**
4.1 Fluidisation characteristics 45
4.1.1 Minimum fluidisation 45
4.1.2 Solids entrainment 46
4.2 Shape analysis results 48
4.2.1 Circularity 49
4.2.2 Other techniques 49
4.3 Understanding particle shape effects in entrainment 50
4.4 Predicting entrainment rates 53

5 Conclusions and Recommendations **56**
5.1 Conclusions 56
5.2 Recommendations 57

A Particle shape description **64**
A.1 Classic techniques 64
A.1.1 Heywood shape factor 65
A.2 Modern techniques 65
A.2.1 Fourier descriptors 65
A.2.2 Fractal dimension 67
A.2.3 Polygonal harmonics 68
A.2.4 Piper's angle and Delta analysis 71
A.2.5 Multi-scale roughness descriptor 73

B Particle data extraction and manipulation **74**
B.1 Image manipulation 75
B.1.1 Grayscale image 75
B.1.2 Black and White Image 75
B.2 Particle shape characterisation 77

C Particle shape analysis results **79**
C.1 Modern techniques 79
C.1.1 Fractal dimension 79
C.1.2 Piper's angle 79
C.1.3 Polygonal harmonics 80

LIST OF FIGURES

2.1 The original classification of powders as done by Geldart (1973) 4
2.2 All the regimes seen in gas–sold fluidisation 6
2.3 The zones found in a fluidised bed and the solids hold up of these zones . 8
2.4 Influence of freeboard height and gas outlet on solids concentration in the freeboard. Square markers indicate a cubic column top with a gas outlet on its side. Triangular markers indicate a pyramidal column top with a gas outlet on its top. From Nakagawa et al. (1994) 12
2.5 Influence of fluidised bed height on the entrainment rate. From Choi et al. (1989) 13
2.6 Influence of fluidised bed height on the entrainment rate. From Baron et al. (1990) 14
2.7 The effect of superficial fluid velocity on the elutriation rate constant. From Tasirin & Geldart (1998) 15
2.8 Increase in entrainment as a result of increased column pressure. From Chan & Knowlton (1984) 15
2.9 The increase in TDH as a result of increased pressure. From Chan & Knowlton (1984) 16
2.10 Temperature effects on the total entrainment rate. From Choi et al. (1998) 17
2.11 Temperature effects on the average diameter for entrained sand particles. From Choi et al. (1998) 18
2.12 Elutriation rate constant as a function of average particle diameter. From Baeyens et al. (1992) 20
2.13 Elutriation rate constant as a function of average particle diameter. From Ma & Kato (1998) 20
2.14 The effect the linear velocity and sphericity of a particle has on the terminal velocity of the same particle 22

2.15 Comparison between the different correlations for the elutriation rate constant $K^*_{i\infty}$ (Numbers in legend refers to correlation number as used in table 2.2) 31
2.16 The ratio of entrainment rates for different sphericities, where the ratio is defined as: $\frac{\text{Entrainment rate of particles with a sphericity of 1}}{\text{Entrainment rate of particles with a sphericity of the value on the x-axis}}$ 33

3.1 A comparison of the difference in appearance between the atomised and the milled FeSi 35
3.2 A schematic of the experimental setup used for all the tests 36
3.3 A comparison for the particle size distribution for all three mixtures used 40
3.4 Indication of how the PSD's of the FeSi mixtures change after an extended period inside the fluidised bed 41
3.5 Comparison between the quality of the images taken with the two types of microscopes 43

4.1 Results of the minimum fluidisation velocity measurements for both the atomised and milled FeSi 45
4.2 Comparison of the entrainment rates for the different solid mixtures. Solid lines represent the average values for the individual mixtures 46
4.3 Prediction of how the entrainment rate should vary as the fraction of atomised FeSi in a FeSi mixture changes according to Geldart et al. (1979). . . 47
4.4 Experimental results of how entrainment rates vary as a function of the fraction of atomised FeSi in the solid mixture. Straight lines represent the theoretical relationships where the PSD is the only factor that influences the entrainment rates. 48
4.5 The circularity of both the atomised and the milled FeSi as a frequency plot. C_{avg} for the atomised FeSi $= 0.782$ and C_{avg} for the milled FeSi $= 0.711$ 50
4.6 Illustration of how the average circularity of entrained solids change as the linear velocity at which they were entrained increases 52
4.7 An indication of how the particle circularity is distributed as a function of particle diameter (Data from sample of atomised FeSi particles). Contours represent normalised frequencies. Note the high circularity of the small particles. 52
4.8 Entrainment rate as measured on the experimental setup together with the predictions of the correlations by Geldart et al. (1979) and Choi et al. (1999) 55

A.1 Example of how the particle shape can affect the periodicity of the rolled out particle perimeter 66

A.2 Example of how the measurement length can affect the perimeter length of an arbitrary figure edge 68
A.3 An illustration of how the step size around the particle affects the perimeter length 69
A.4 A log-log plot used to calculate the fractal dimension 69
A.5 Illustration of third and fourth harmonics for a particle 70
A.6 Illustration of how Piper's angles are measured 72
A.7 An illustration of how Piper's angle can be lacking as a shape descriptor 72

B.1 Manipulation of image obtained from microscope from full colour image (a) to a greyscale image (b) 74
B.2 Bimodal Gaussian distribution for the range of intensities in figure B.1(b) 76
B.3 Noisy black and white image (a) obtained after thresholding and cleaned black and white image (b) 76
B.4 Extracted particle border of one of the particles in figure B.3. Note that the dimension of the radius is μm 77
B.5 A schematic illustration of how the particle perimeter is approximated with a series of lines of equal length 78

C.1 The fractal dimensions for both the atomised and milled FeSi expressed in a frequency plot. $D_{f_{avg}}$ for milled FeSi = 1.056 and $D_{f_{avg}}$ for atomised FeSi = 1.065 80
C.2 Frequency plot of the Piper's angles for the atomised and milled FeSi batches 81
C.3 Frequency plot of the persistence of the second polygonal harmonic . . . 81
C.4 Frequency plot of the persistence of the third polygonal harmonic 82
C.5 Frequency plot of the persistence of the fourth polygonal harmonic 82
C.6 Frequency plot of the persistence of the fifth polygonal harmonic 83

LIST OF TABLES

2.1 Commonly used correlations to predict the entrainment flux at the fluidised bed surface, E_0 26
2.2 Commonly used correlations for the Elutriation rate constant $K^*_{i\infty}$ 28

3.1 Properties of particle mixtures used inside fluidised bed reactor 34
3.2 Detail information of differential pressure drop transmitters 37
3.3 Operating conditions used for the fluidised bed 38
3.4 Relative errors in entrainment for different particle mixtures with respect to the average value of entrainment for the different particle mixtures . . 39
3.5 Fines fraction of different particle mixtures 40
3.6 Relative difference in entrainment for different fixed bed heights with respect to the average value of entrainment at the normal fixed bed height 42

4.1 Comparison between the performance of the different shape description techniques 49
4.2 Performance of different elutriation rate correlations in predicting the experimental entrainment rates for the different solid mixtures 54

A.1 Harmonic characteristics for isometric shapes (From Clark (1987)) 71

NOMENCLATURE

C	Circularity of particle	-
ϵ	Voidage of fluidised bed, defined as the fraction of the total control volume that is not filled with solids	-
μ	Dynamic viscosity of fluid	Pa.s
ϕ_i	Harmonic phase angle	Radians
Ψ	Sphericity of particle	-
Ψ_w	Working sphericity	-
Ψ_{op}	Operational sphericity	-
θ	Angle used in particle edge tracking	Radians
A	Cross sectional area of bed	m^2
A_i	Harmonic amplitude in Fourier expansion, where i refers to the harmonic order	-
a_i	Exponential decay coefficient for entrained particles	m^{-1}
A_p	Surface area of particle	m^2
B	Constant used in entrainment rate constant correlation by Merrick & Highley (1974)	-
b	Breadth of particle	m
C_d	Drag coefficient	-
D	Diameter of fluidised bed reactor	m

d_a	Projected area diameter	m
d_b	Bubble diameter	m
D_f	Fractal dimension	-
D_h	Hydraulic diameter of column $(\frac{4A}{\text{Circumference}})$	m
d_s	Surface diameter of particle	m
d_v	Volume diameter of particle	m
d_{eq}	Equivalent diameter	m
$d_{p_{crit}}$	Critical particle diameter	m
d_{st}	Free-falling diameter of particle	m
d_{sv}	Sauter diameter of particle	m
e_1	Flatness ratio	-
e_2	Elongation ratio	-
E_∞	Total entrainment rate	$\mathrm{kg/m^2s}$
E_{i0}	Entrainment flux of solids at fluidised bed surface	$\mathrm{kg/m^2s}$
E_{ih}	Entrainment flux for component i at a height above the distributor, h	$\mathrm{kg/m^2s}$
F_d	Drag force per particle projection area	Pa
F_g	Gravity force per particle projection area	Pa
g	Gravitational acceleration constant	$\mathrm{m/s^2}$
G_{s_i}	Choking load for particles of component i	$\mathrm{kg/m^2s}$
k	Heywood shape factor	-
K_{ih}^*	Elutriation rate constant for component i, at a height above the distributor, h	$\mathrm{kg/m^2s}$
k_e	Heywood shape factor for isometric particle	-
l	Length of particle	m
M_B	Mass of solids in the fluidised bed	kg
M_{i_t}	Mass of solids of component i captured after time t	kg

n	Harmonic order in Fourier expansion	-
n	Order of polygonal harmonic	-
N^*_{coh}	Cohesion number used to calculate critical particle diameter	-
P_n	Harmonic persistence of the n^{th} order	-
S_p	Surface area of particle	m^2
t	Thickness of particle, used in equation 2.14	m
t	Time	s
U	Superficial velocity of fluid through column	m/s
U_c	Linear velocity where standard deviation in pressure fluctuations over the bed is at a maximum	m/s
U_k	Linear velocity at the onset of turbulent fluidisation	m/s
U_r	Relative linear velocity of particle to fluid	m/s
U_t	Terminal velocity of particle	m/s
U_{mf}	Minimum fluidisation velocity	m/s
U_{t_i}	Terminal velocity for particles of component i	m/s
U_{tr}	Linear velocity that characterise the onset of the fast fluidisation regime in which significant solid transport occurs	m/s
V_p	Volume of particle	m^3
V_p	Volume of particle	m^3
x_{B_i0}	Fraction of solids of component i present in fluidised bed at time 0	-
x_{B_i}	Mass fraction of particles of component i in the fluidised bed	-
ϵ_{mf}	Voidage in fluidised bed at minimum fluidisation conditions	-
ρ_f	Density of the fluid	kg/m^3
ρ_s	Density of the particle	kg/m^3
Ga	Galileo number calculated as $\frac{d_p^3(\rho_s-\rho_f)g}{\mu^2}$	-
ML	Measured length, used in fractal dimension calculation	m

Re_c	Reynolds number for the fluidised bed column, calculated as $\frac{D\,\rho_f\,U}{\mu}$	-
Re_p	Particle Reynolds number	-
Re_t	Reynolds number for particles at their terminal velocity, calculated as $\frac{d_p\,\rho_f\,U_t}{\mu}$	-
S	Slope of SL vs ML, used in fractal dimension calculation	-
SL	Step length, used in fractal dimension calculation	m

CHAPTER 1

Introduction

Fluidised beds are one of the standard solid–fluid contacting systems where the fluid flows upwards through the solids at such a velocity that the gravitational force on the solids is overcome and the solids can drift in the upward flowing fluid. This causes the solids to behave as a liquid. Fluidised beds are one of the most frequently used solid–gas contacting systems in a vast range of industries. The range of uses for fluidised beds include chemical and mineral processing, gasification and combustion for power generation, environmental technologies, in the petrochemical industry as crackers and reactors, pharmaceuticals, biotechnology and other solids handling industries (Yang, 2003: p.iii). Fluidised beds have many advantages above other solid–fluid contacting systems such as the ease in solids handling because of the liquid-like behaviour, the isothermal operation of a fluidised bed and the excellent heat and mass transfer. The disadvantages of fluidised beds include the fact that the fluidised bed approaches a continues stirred tank reactor rather than a plug flow reactor, the large amount of attrition caused by the vigorous mixing and high velocities of the solids and lastly the loss of solids from the fluidised bed by means of entrainment and elutriation.

High temperature Fischer-Tropsch (HTFT) reactors are one of the commonly used gas–solid fluidised beds where entrainment of the solid catalyst needs to be understood (Sookai et al., 2005). In the HTFT reactors the properties of the catalyst change as the time on stream of the catalyst increases. These changes include a decrease in density, a shift in the particle size distribution (PSD) towards a lower average particle diameter and a shift in sphericity towards more spherical particles. This occurs as a result of carbon deposition on the particles as well as attrition inside the bed and in the cyclones (Smit et al., 2004). The effects of the changes in particle size and density on entrainment rates are well documented in literature (Baeyens et al., 1992; Ma & Kato, 1998). However, no quantitative studies have been done on the effect of particle shape on entrainment, where only the particle shape was varied while the size and density were kept constant.

A wide range of correlations exists in literature for predicting entrainment from a fluidised bed. These correlations are mostly empirical with little theoretical basis and therefore it is important to use a correlation that was developed for a system similar to the one of which the prediction is required (Yang, 2003: p.121). The problem with this heuristic is that most of these correlations were derived on either sand, fluid catalytic cracking catalyst (FCC) or glass beads (Zenz & Weil, 1958; Wen & Hashinger, 1960; Tanaka et al., 1972; Colakyan & Levenspiel, 1984; Baeyens et al., 1992; Nakagawa et al., 1994; Tasirin & Geldart, 1998). It is therefore hard to find a similar system for HTFT reactors, as these reactors use an iron based catalyst.

Most of the correlations in literature do take particle shape into account by using the terminal velocity in the correlation. It is therefore assumed that the terminal velocity of a single particle is sufficient to include the effect of particle shape on entrainment rate. However, few of these papers report a particle sphericity and it is difficult to determine how the sphericity used to calculate the terminal velocity was calculated, if at all and if the sphericity was not just assumed to be 1.

The aim of this study is to investigate whether particle shape has a significant effect on entrainment rate. Furthermore the ability of existing correlations to predict the entrainment rate from fluidised beds that uses iron-based solids which lies on the Geldart A-B border, similar to the HTFT catalyst, must be evaluated. Specifically whether these correlations are able to quantify the effect of particle shape on entrainment. In order to do so, a suitable shape description technique should be found that is able to differentiate properly between particle shapes.

The investigation was done in a 140 mm perspex column. Two mixtures of Ferrosilicon (FeSi) with similar PSD's and densities to that of the HTFT catalyst were used. The atomised FeSi contained mostly smooth, spherical particles, while the milled FeSi had rough, irregular flake-like particles. Both these mixtures had similar average particle diameters of ranging from 38 μm to 50 μm and the only property that differed significantly between the mixtures was the particle shape. Compressed air was used as the fluidising medium. The range of superficial velocities in which the entrainment rates were measured ensured that all tests were done in the bubbling regime. All entrainment measurements were done at ambient conditions. All the particle shape quantifications were done with computerised analysis of particle images taken with a scanning electron microscope (SEM).

CHAPTER 2

Literature Study

2.1 Fluidisation

For fluidisation to take place, three critical elements are required:

- A vessel in which the fluidisation can occur
- Solid packing inside the vessel
- A fluid (One or two phases) that flows upward through the packing in the vessel

Fluid flow through a packed bed has been studied by Ergun (1952) who found that the pressure drop through the bed is proportionate to the flow rate through the bed. This pressure drop is the sum of the viscous and kinetic energy losses due to frictional drag of the fluid on the packing in the bed. Two general arrangements are normally used when passing a fluid through a packed bed. Firstly, where the drag on the packing and the weight of the packing is in the same direction. In this case the direction of the fluid flow is downward. Secondly where the drag on the packing and the weight of the packing is in opposite directions, which means that the direction of the fluid flow should be upward. Fluidisation can only be achieved in the second case.

To achieve fluidisation, the flow rate of the fluid has to be increased to such a velocity where the drag force on the packing in the bed surpasses the weight of the particles in the bed. At the point where the drag force on the packing is equal to the weight of the packing, the bed is in a state of incipient fluidisation, or minimum fluidisation. With a further increase in flow rate of the fluid, the bed will expand as particles start to drift freely in the fluid with frequent collisions between the particles.

2.1.1 Solid classification

Different types of solids fluidise differently as many different factors such as drag, particle interactions, etc influence the behaviour of these particles during fluidisation. Geldart (1973) was the first to classify the fluidisation behaviour of the different types of solids in a gas and group them into four different types, namely the Geldart A, B, C and D powders. An illustration of the layout of the famous Geldart chart can be seen in figure 2.1.

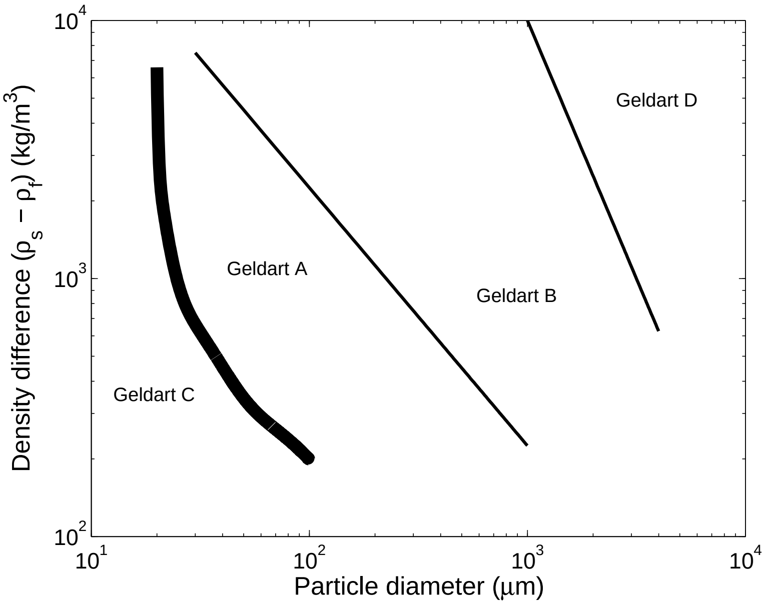

Figure 2.1: The original classification of powders as done by Geldart (1973)

Geldart A powders

These powders fluidise easily and homogeneously at low gas flow rates. The bed will expand uniformly up to the point where the minimum bubbling velocity is reached, which is usually higher than the minimum fluidisation velocity. At flow rates higher than the minimum bubbling velocity, Geldart A powders will exhibit a maximum bubble size. Note that the minimum bubbling velocity refers to the linear velocity at which bubbles will start to appear inside the fluidised bed. These bubbles are similar to bubbles appearing in a liquid through which a gas is bubbled.

Geldart B powders

Similar in behaviour to sand, these powders fluidise well but not homogeneously. Bubbles start to appear as soon as the minimum fluidisation velocity is passed. These bubbles will grow in size up to bed diameter, when the bed will start to slug.

Geldart C powders

This group consist of very fine, dense powders. Normal fluidisation with Geldart C powders tend to be troublesome, as the gas tend to channel through the bed. This difficulty in fluidisation is as a result of the large inter-particle forces associated with such small solids.

Geldart D powders

These particles have large diameters compared to the other Geldart classifications. A stable spouted bed can easily be formed with these powders, but it is hard to fluidise Geldart D powders normally.

This chart has been further developed by various authors to improve it so to ensure that it includes higher pressures and fluids other than air, since Geldart only did his classification with air at ambient conditions. A review of these methods can be found in Yang (2007), with an updated chart able to classify powders within a much higher range of conditions.

2.1.2 Fluidisation regimes

Up to the point of minimum fluidisation gas–solid and liquid–solid fluidisation is very similar with respect to hydrodynamics. Beyond minimum fluidisation the major differences becomes apparent, with the biggest difference being the regimes of fluidisation. These regimes can be seen in figure 2.2. Liquid–solid fluidisation exhibit homogeneous fluidisation in almost all the cases, while gas–solid fluidisation rarely display homogeneous fluidisation and in those few cases, the range of flow rates for which homogeneous fluidisation presents itself is very narrow (Harrison et al., 1961).

Minimum and particulate fluidisation

Minimum or incipient fluidisation occurs at the point where the upward drag on the solid packing is equal to the weight of the packing. The height of the bed will be the same as for a fixed bed, or marginally higher than that of the fixed bed. The particles move about slightly, but only on a small scale. In most cases the particles just ‘vibrate’ in their local positions in the bed. With gas–solid fluidisation, increasing the flow rate will cause a bed of Geldart A powder to expand smoothly. The other powders do not exhibit this type of fluidisation. This behaviour can also be seen with liquid–solid fluidisation (Yang, 2003: p.58).

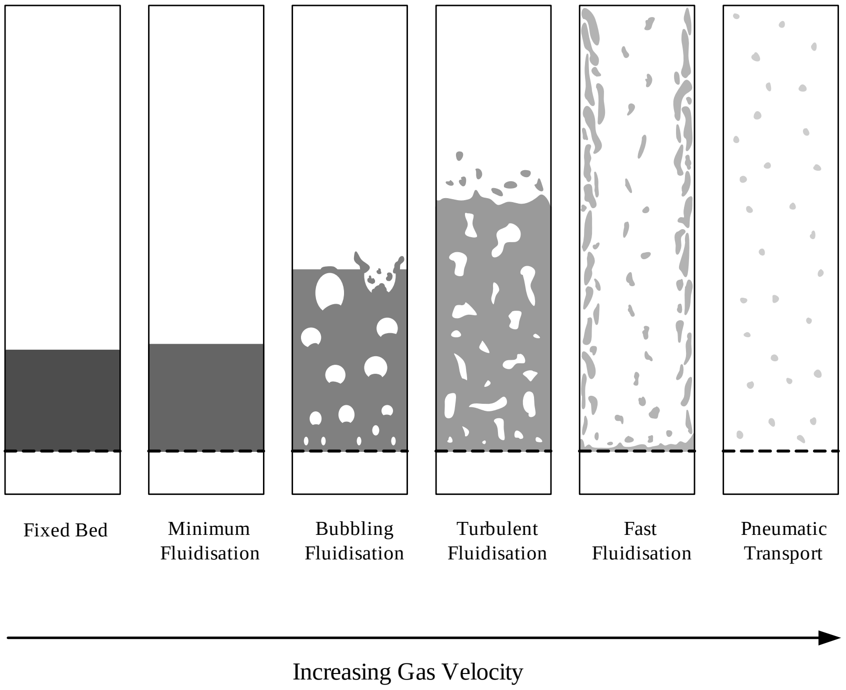

Figure 2.2: All the regimes seen in gas–sold fluidisation

Bubbling fluidisation

As the gas flow rate is increased beyond minimum fluidisation, small bubbles will start to appear in the smoothly fluidised bed. This point where bubbles start to appear is called the minimum bubbling velocity. Geldart B and D particles does not exhibit particulate fluidisation behaviour. Therefore the minimum bubbling velocity and the minimum fluidisation velocity is the same for Geldart B and D powders. As soon as the flow rate is increased beyond the point of minimum fluidisation with these powders, bubbles start to emerge from the bed surface. Therefore the excess gas that is not used to keep the bed at the minimum fluidisation condition, pass through the bed in the form of bubbles, or big fast moving voids that contain little to no solids. Geldart A powders also show bubbling behaviour, but for Geldart A powders, the minimum bubbling velocity is not equal to the minimum fluidisation velocity. Small bubbles form above the distributor and as they move through the bed they start to coalesce to grow larger. In a fluidised bed of Geldart A powder, the bubbles reach a stable size from which they will not grow further (Kunii & Levenspiel, 1991: p.130). The height above the distributor where this occurs is often less than 10 cm. Stable bubble sizes do not exist for Geldart B and D solids. With these powders the bubbles will increase to grow as they move through the bed until slugs are formed. These slugs, which have bubble diameters of 67% or more of the bed diameter, cause large, regular pressure fluctuations in the bed. A fluidised bed that operates in the bubbling regime can be divided into two 'phases'. Firstly a dense phase that contains a high concentration of solids. The dense phase has similar hydrodynamics to a fluidised bed at minimum fluidisation conditions. Secondly there exists a lean phase that contain little or no solids. The bubbles of a bubbling fluidised bed are the main constituent of the lean phase.

Turbulent fluidisation

With an even further increase in the flow rate, the bubbles grow bigger up to a point where the flow rate does not influence the bubble size anymore. These bubbles will cause large deviations in the pressure drop over the fluidised bed. To describe the transition from bubbling to turbulent fluidisation, two characteristic velocities described by Yerushalmi & Cankurt (1979) are required. The first of the velocities, U_c, is used to describe the flow rate at which the standard deviation of the pressure fluctuations over the fluidised bed is at a maximum. If the flow rate is increased beyond U_c, the standard deviation in the pressure drop start to decrease, as the larger bubbles associated with U_c start to break up into smaller bubbles. The second characteristic velocity, U_k, describes the onset of turbulent fluidisation. At this point the standard deviation in the pressure drop reaches a steady state. A fluidised bed in the turbulent regime is much more homogeneous than one in the bubbling regime. There exists a high interaction between the lean and dense phases of the bed, due to the constant coalescence and break-up of bubbles in the fluidised bed.

Fast fluidisation and Pneumatic transport

The fast fluidisation regime is essentially a regime where the solids in the fluidised bed is in pneumatic transport. This regime can be reached by increasing the flow rate of the gas beyond U_k up to U_{tr}, where U_{tr} is the transport velocity for the solids. This transport velocity is significantly larger than the terminal velocity when fluidising Geldart A and B powders, but U_k and U_{tr} are more or less equal when fluidising Geldart D powders. This means that there is a very narrow range of velocities in Geldart D powders where turbulent fluidisation occurs. These powders proceed from bubbling fluidisation straight to fast fluidisation. Fast fluidisation cannot be achieved if no solids return is present in the fluidised bed, otherwise the contents of the bed will be lost after a short period of operation. The main difference between fast fluidisation and pneumatic transport is that fast fluidisation is operated at a flow rate closer to U_{tr}, which results in a dense phase and a lean phase inside the bed, while pneumatic transport has a homogeneous distribution of solids throughout the bed. In the case of fast fluidisation, the dense phase, or 'annulus' is close to the wall of the vessel with solids flowing down while the lean phase, or 'core' is in the centre of the vessel where the solids flow up (Yang, 2003: p.62).

2.1.3 Zones in a fluidised bed

In a fluidised bed reactor distinct zones can be found. These zones all have their own specific properties and unique hydrodynamic behaviour, which are used to identify the zones and which influence the conditions and events inside the zones. An illustration of the most important zones can be seen in figure 2.3. These are the most important zones in a fluidised bed. The dense bed is found at the bottom of the vessel and this is the zone in the fluidised bed where most of the particles are found. The dense bed is where all the bubbles are formed which eject the solids out of the dense bed. The dense bed is the zone of the fluidised bed with the highest solid hold-up and lowest voidage, ϵ. The interface between the dense bed and the zone above the dense bed is called the splash zone and is in appearance very similar to the surface of a boiling liquid. It is in this zone where all the solids are ejected into the freeboard. When the fluidised bed is in the turbulent or fast fluidisation regime, the splash zone is difficult or even impossible to distinguish from the dense bed. The solid concentration in the splash zone has a very sharp exponential decay, as most of the clumps of solids that gets ejected into the freeboard falls back to the dense bed. The zone above the splash zone has a more gradual decrease in solids concentration up to a point where the solids concentration remains constant for all practical purposes. This distance from the bed surface up to the point where the solids concentration remains constant is called the transport disengagement height (TDH). The last important term

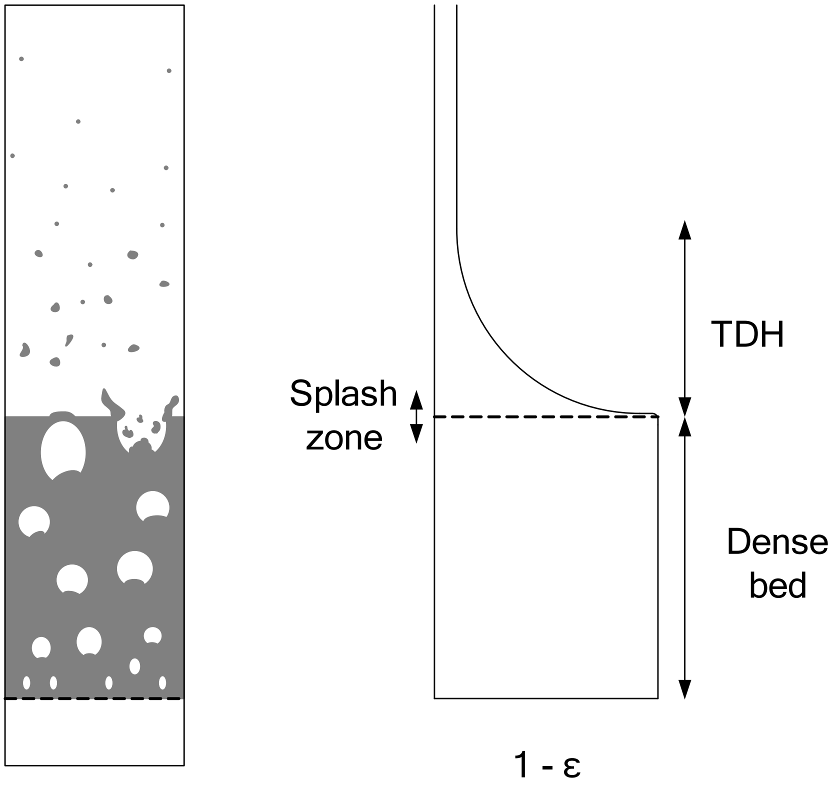

Figure 2.3: The zones found in a fluidised bed and the solids hold up of these zones

to be aware of when considering the zones in a fluidised bed is the freeboard, which refers to the distance above the dense bed, up to the gas exit out of the vessel (Yang, 2003: p.114).

2.2 Entrainment

Entrainment is defined as the removal of solids from a fluidised bed and the consequent transport of these solids along the freeboard out of the vessel (Yang, 2003). The loss of the solids from the fluidised bed can result in major financial costs, as the solids are typically expensive. The removal of the solids from the exit gas by means of filters and cyclones also result in additional costs, as the equipment used to remove the solids can be expensive and generally have large operating costs associated with them (Zenz & Weil, 1958).

2.2.1 Particle transport into freeboard

For solids to be entrained they have to leave the dense bed and enter the freeboard. The gas bubbles bursting at the bed surface are responsible for this. It is well known that the pressure inside a bubble is higher than the ambient pressure at the bed surface (Kunii & Levenspiel, 1991: p.118). The ejection of the particles into the freeboard by the exploding bubble is known to occur by one of four mechanisms (Levy et al., 1983). The most common mechanism is when a single bubble bursts through the bed surface and the roof of the bubble is thrown into the freeboard. The rest of the mechanisms rely on the fact that two bubbles coalesce at the bed surface. When this happens, one of three events can occur. The most common event is that the wake of the trailing bubble is energetically ejected into the freeboard, reaching a much higher height than the height reached by the exploding bubble roof. Another mechanism is when the two bubbles coalesce at the bed surface and the middle layer between the two bubbles is ejected into the freeboard. This does not occur very often. The last mechanism is when two bubbles coalesce and a route forms for a jet stream of gas to pass through. This gas jet entrains particles in its passage and transports the particles to relatively high distances above the bed surface. A big difference between bubble roof particles and bubble wake particles is that the particles ejected into the freeboard from the roof is highly dispersed through the freeboard, while the particles from the wake remains in a closely packed clump (Yang, 2003: p.115). The presence of bubbles can be found in all the fluidisation regimes where the fluidised bed can be divided into a lean and a dense phase. These mechanisms described by Levy et al. (1983) can therefore still be applied to the turbulent regime not just to the bubbling regime.

The velocity of these particles as they are leaving the dense bed and entering the fluidised bed is about the same as the bubble rise velocity (Peters et al., 1983), which is normally much higher than the superficial velocity in the bed. This explains why the particles can enter the freeboard and travel upward for a distance above the dense bed before they fall back onto the dense bed even when the superficial gas velocity is too low to entrain the particles.

2.2.2 Flow structure in freeboard

When the solids enter the freeboard of the fluidised bed reactor, they can either be carried away with the gas stream and leave the reactor, or they can fall back to the dense bed surface and enter the dense bed again. If the particles are all considered on their own with a simple ballistic model it is expected that the concentration of the particles in the freeboard will decrease rapidly to a constant value for the fraction of entrainable particles. Experimental results show a different profile than expected (Geldart & Pope, 1983). Particles with a terminal velocity higher than the superficial fluid are entrained when it is expected that they should settle out and return to the dense bed. The concentration of the very fine particles, that should all be entrained, decreases as the height of the freeboard increases, while it is expected that the concentration will remain constant (Geldart & Pope, 1983). These results can be explained by particle-particle interactions. It is known that the particles do not move about individually, but that they clump together in clusters (Yang, 2003: p.115). These clusters have the ability to ‘carry’ the heavier particles that will not be entrained if they were in the freeboard on their own. The clusters also act as bigger particles, which explains why even the fines concentration in the freeboard decreases when it should remain constant, as all the fines are entrainable.

Solids are entrained as a result of the fluid flowing through the freeboard. Therefore it is important to not only consider the effects of solids on each other, but also the fluid flow pattern. A large factor that influences the flow pattern of the fluid is the Reynolds number based on the superficial fluid flow. If the superficial fluid flow is in the laminar regime, the large particles will easily rise in the centre and relatively small particles will move down along the sides as a result of the velocity profile attributed to laminar flow. This is not really seen in turbulent flow (Yang, 2003: p.116). The flow pattern of the fluid through the freeboard is unfortunately not as easy to describe as plug flow, that is affected only by the flow regime of the fluid. It has been found by various investigators that rapid fluctuations exists in the fluid flow in the freeboard as a result of the bubbles exploding at the dense bed surface (Yórquez-Ramírez & Duursma, 2001; Du et al., 2005; Chaplin et al., 2005). The methods by which the bubbles disturb the fluid flow in the freeboard have been explained in two ways. In the past it has always been accepted that the bubbles maintain their identity, even after entering the freeboard. The fluid will therefore continue to recirculate in these 'ghost bubbles' as it had done inside the bubbles in the dense bed. The recirculation inside the bubbles enables these ghost bubbles to entrain the surrounding fluid in the freeboard. This causes the ghost bubbles to loose their speed and identity so that they assimilate into the surrounding freeboard fluid (Pemberton & Davidson, 1984).

However, this theory has been suggested to be false (Yórquez-Ramírez & Duursma, 2000, 2001). Pemberton & Davidson (1984) used a hot wire anemometer to measure the turbulence, and the ghost bubbles, in the freeboard. The problem with this method is that the fluid flow and ghost bubbles can only be measured one at a time and no overall picture of what happens in the freeboard can be obtained from this method. Yórquez-Ramírez & Duursma (2000, 2001) used particle image velocimetry (PIV). The advantage of this method is that an overall picture can be obtained from what happens in the entire freeboard of the fluidised bed. The effect of all the bubbles bursting in the freeboard on the fluid flow structure can be seen together. They found that the fluid jets from the exploding bubbles. As the velocity of the jet is much higher than the velocity of the fluid in the freeboard, vortex rings are created as a result of the shear between the jet and the surrounding fluid. These vortex rings and eddies that are induced by the bursting bubbles, are responsible for the chaotic turbulence in the freeboard.

2.3 Factors influencing entrainment and elutriation

Fluidised bed reactors are operated over a wide range of conditions in various different processes. It is therefore important to know how the different factors can influence the entrainment and elutriation from the fluidised bed. The following factors have been identified as the major influencing characteristics.

2.3.1 Effect of reactor properties

In the various different applications of fluidised beds, the reactor properties might vary significantly between the different applications. It is therefore important to know how the different reactor properties will influence entrainment and elutriation.

Effect of freeboard height and shape

A very chaotic and violent environment exists at the bed surface of a fluidised bed as a result of bubbles bursting and turbulent gas vortexes. This turbulent environment is therefore responsible for a high entrainment rate at the bed surface. As the height above the bed surface increases, these turbulent occurrences die out to ensure a more homogeneous flow pattern. It is therefore easy to understand why the entrainment rate at the bed surface is so high and why it will decrease rapidly to a constant value. The entrainment rate at a specific height will be directly proportional to the particle concentration at that height. Therefore the concentration profile of the solids in the freeboard will follow the same trend as the entrainment rate. This height at which the entrainment rate remains constant is called the Transport disengagement height (TDH). Nakagawa et al. (1994) found that the geometry of the gas outlet does not influence the elutriation rate at all. These results can be seen in figure 2.4. The good repeatability of these results gives an indication that the position of the gas outlet at the top of the fluidised bed does not influence the elutriation rate, as long as the outlet is above the TDH.

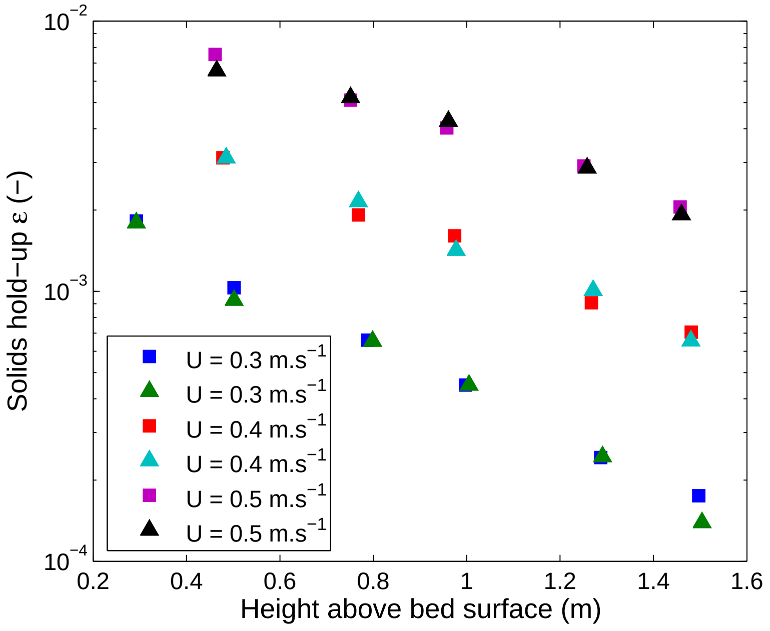

Figure 2.4: Influence of freeboard height and gas outlet on solids concentration in the freeboard. Square markers indicate a cubic column top with a gas outlet on its side. Triangular markers indicate a pyramidal column top with a gas outlet on its top. From Nakagawa et al. (1994)

Effect of packed bed height

It has been stated in previous sections that the main mechanism by which the solids are transported into the freeboard is by the bursting of bubbles at the bed surface. It is also well known that the bubble diameters increase as they move up through the bed, up to the height where a stable bubble size is reached (Only Geldart A powders have a stable bubble size, the bubbles in other Geldart powders increase in size until they reach the reactor diameter). Various correlations exist that describes this, for example the one developed by Rowe (1976). In this correlation the relationship between the bubble diameter and the height above the distributor can be given by:

$$d_b \propto h^{\frac{3}{4}} \tag{2.1}$$

It is therefore expected that the packed bed height ought to influence the entrainment rate into the freeboard of the fluidised bed. This has been investigated by Choi et al. (1989) as well as Baron et al. (1990).

Different results were obtained by the two research groups. Choi et al. (1989) found no discernible trends in the effect of the bed height on the entrainment rate, as can be seen in figure 2.5. However, this study was not done specifically to see how the bed height might influence the entrainment rate. These results were only obtained in a broader study on fluidised bed combustors. Therefore some of the critical parameters might not have been kept constant to properly investigate the effect of bed height on entrainment rate.

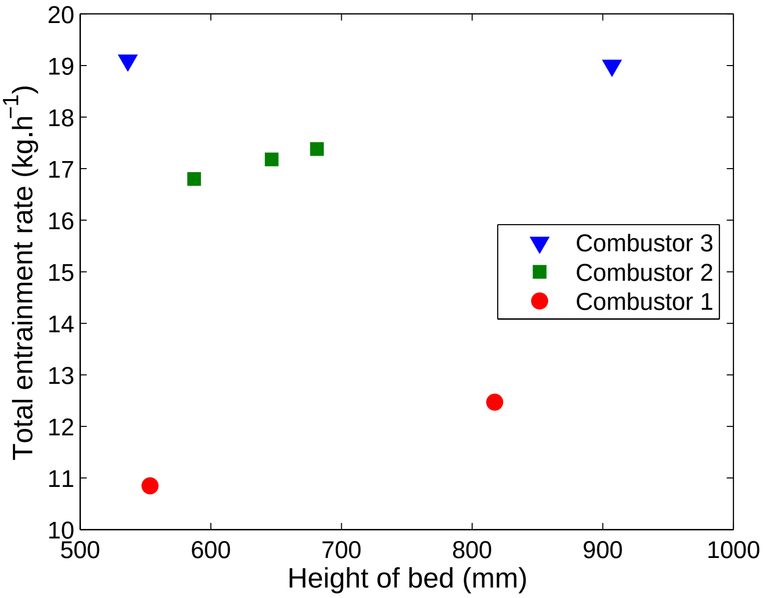

Figure 2.5: Influence of fluidised bed height on the entrainment rate. From Choi et al. (1989)

As can be seen in figure 2.6, the results obtained by Baron et al. (1990) shows the expected trend of increased entrainment with increased bed height. From these results it can be seen that even though the entrainment rate increases with bed height, the amount by which the entrainment rate increases as a result of increased bed height, compared to the amount by which the entrainment rate increases as a result of other factors, is almost insignificant. What can be seen from figure 2.6 is that at high superficial velocities, the effect of the bed height is slightly stronger.

2.3.2 Effect of fluid properties

In fluidised beds, the solid particles are fluidised with a wide range of different fluids. These fluids have properties that can differ in order between the different fluids. Taking this into consideration, it is important to know exactly how these properties influence

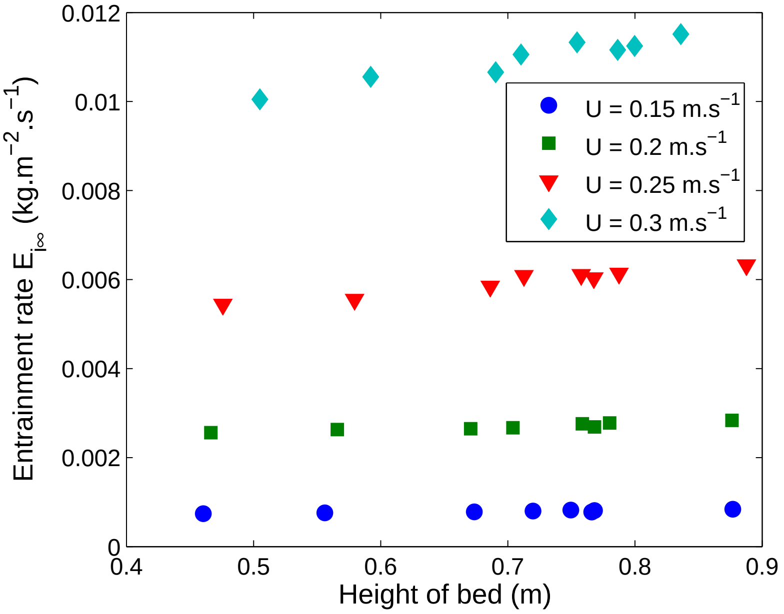

Figure 2.6: Influence of fluidised bed height on the entrainment rate. From Baron et al. (1990)

the entrainment and elutriation rates.

Effect of linear velocity

Particles are normally entrained and elutriated because the superficial velocity is larger than the particle terminal velocity. A high superficial velocity will also increase the amount of particles being ejected into the freeboard. It is therefore easy to understand why a high superficial velocity will have a large entrainment and consequently a large elutriation rate. This effect can be seen in figures 2.4, 2.6 and 2.7, 2.13.

Effect of pressure

As pressure in a gas is increased, the gas becomes more dense. Therefore gas at a higher pressure, or more a dense gas, will have a better capability to carry the solids away. In addition, Chan & Knowlton (1984) found that the TDH will also increase linearly as pressure is increased. These results can be seen in figures 2.8 and 2.9. Another event that occurs when the pressure is increased, is that the diameter of the bubbles in the column decreases (Cai et al., 1994). This will result in less solids that will be ejected into the freeboard as a result of the smaller bubbles. There are therefore two counteracting effects when the pressure is increased.

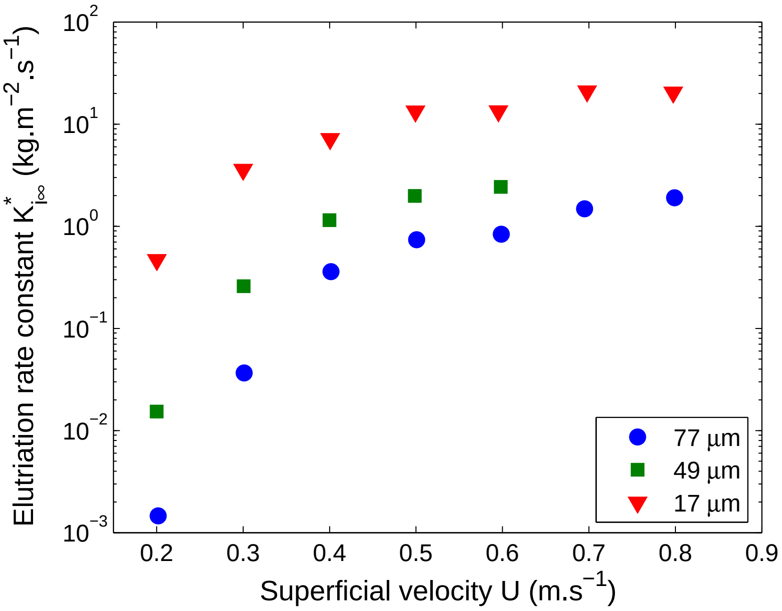

Figure 2.7: The effect of superficial fluid velocity on the elutriation rate constant. From Tasirin & Geldart (1998)

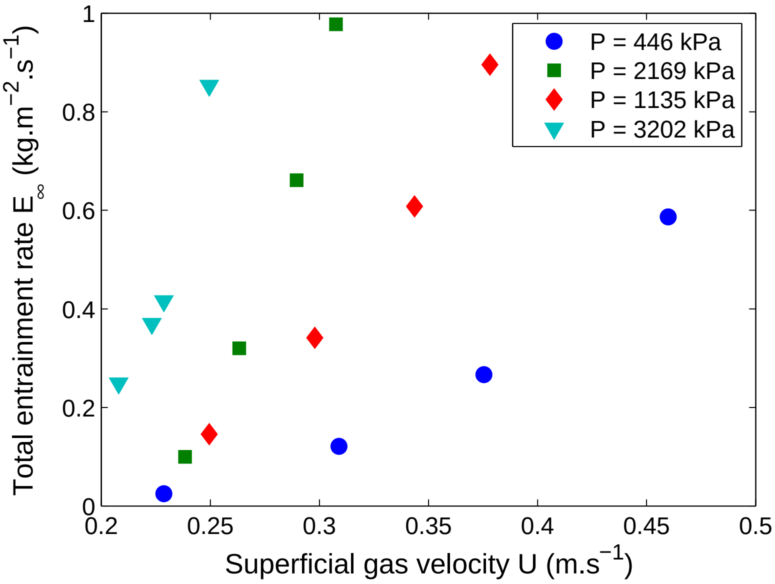

Figure 2.8: Increase in entrainment as a result of increased column pressure. From Chan & Knowlton (1984)

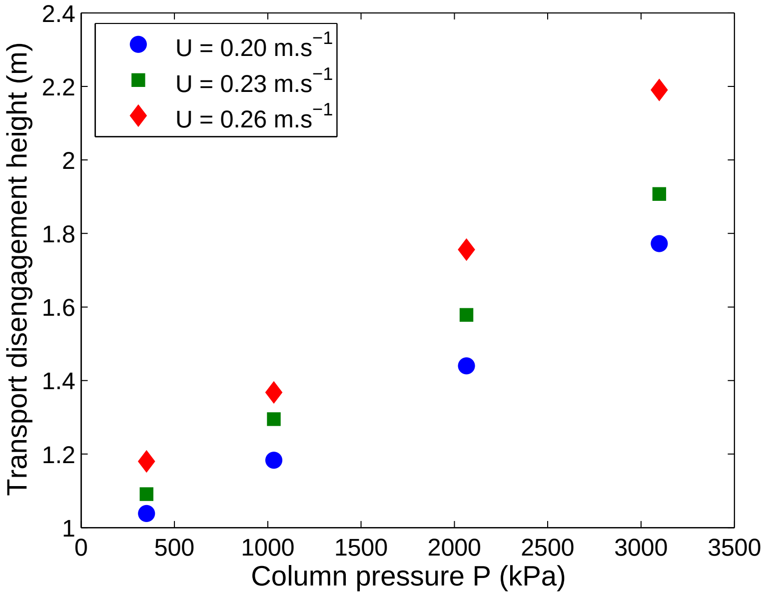

Figure 2.9: The increase in TDH as a result of increased pressure. From Chan & Knowlton (1984)

Effect of temperature

Temperature has a large effect on the fluid properties, as well as the properties of some solids, depending on the composition. The effect of temperature should therefore not be discarded just because it is possible to calculate the new gas properties at the new temperature. The effect of the temperature on the fluidised bed as a whole should be understood. George & Grace (1981) did an investigation on a pilot scale fluidised bed, and one of the factors they investigated was the effect of the temperature on elutriation. They only operated in a small range of 300 K to 445 K and found no temperature effects. Choi et al. (1989) found that entrainment rate decreased as the temperature increased, but they worked in a temperature range of 1050 K to 1200 K in a fluidised bed combustor. The effect of temperature on entrainment and elutriation seems therefore to be dependant on the absolute value of the temperature at which the fluidised bed is operated. Choi et al. (1998) did an investigation over a wide range of temperatures from 273 K to 873 K with different types of solids. Some of the results obtained by Choi et al. (1998) can be seen in figure 2.10. These results show why some groups report an increase in the total entrainment rate while others report a decrease in the entrainment rate. Choi et al. (1998) also found that the diameter of the averaged entrained particle changes with temperature, as can be seen in figure 2.11. These results can be an indication of the interaction between the increase in viscosity and the decrease in density as temperature increases. That might explain why the average diameter for the entrained particles will decrease before it will increase. The work done by Choi et al. (1998) gives an indication of what trend will be seen in all particles. Care should be taken however, as the temperature profile for different kinds of solids might vary significantly, and therefore it could lead to big errors if the temperature profile determined for one type of solid is used for another type of solid.

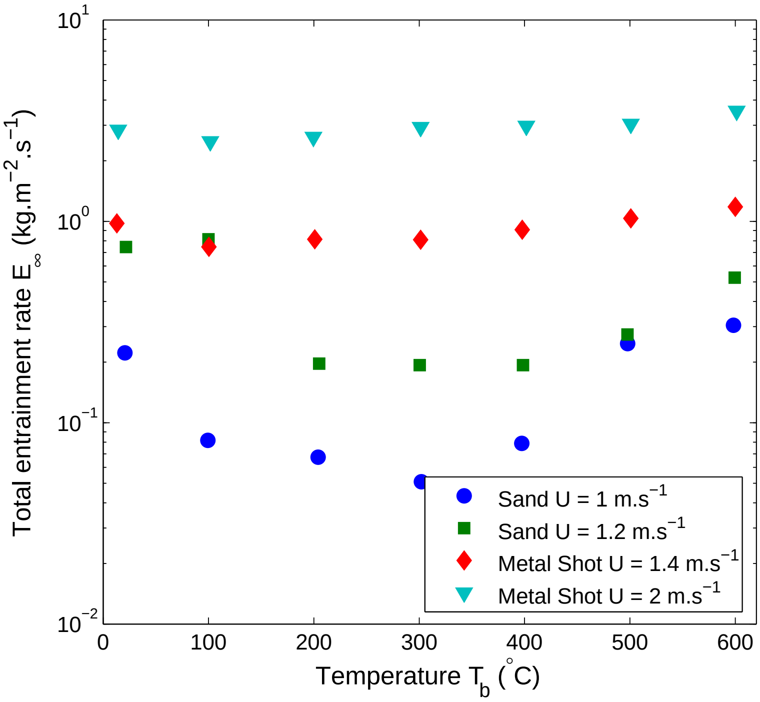

Figure 2.10: Temperature effects on the total entrainment rate. From Choi et al. (1998)

2.3.3 Effect of particle properties

Entrainment can be affected by different properties of the solid particles that are used in the fluidised bed. Of these properties, the most important are the particle diameter, the particle density and the particle shape. The influences of particle density on entrainment is in most cases intuitively obvious, the more dense the particle, the higher the terminal velocity, which results in a lower entrainment. There exist cases however where more dense particles causes the formation of larger bubbles which ejects more solids into the freeboard and results in a higher entrainment rate than expected (Smit et al., 2004). This is the exception on the rule however. The effect of particle density will therefore not be discussed any further.

Effect of particle diameter

When particle size is considered, the biggest variable that influences the entrainment and elutriation from the fluidised bed is the particle diameter. Firstly it is important to classify the method by which the particle diameter is calculated. Various methods exist

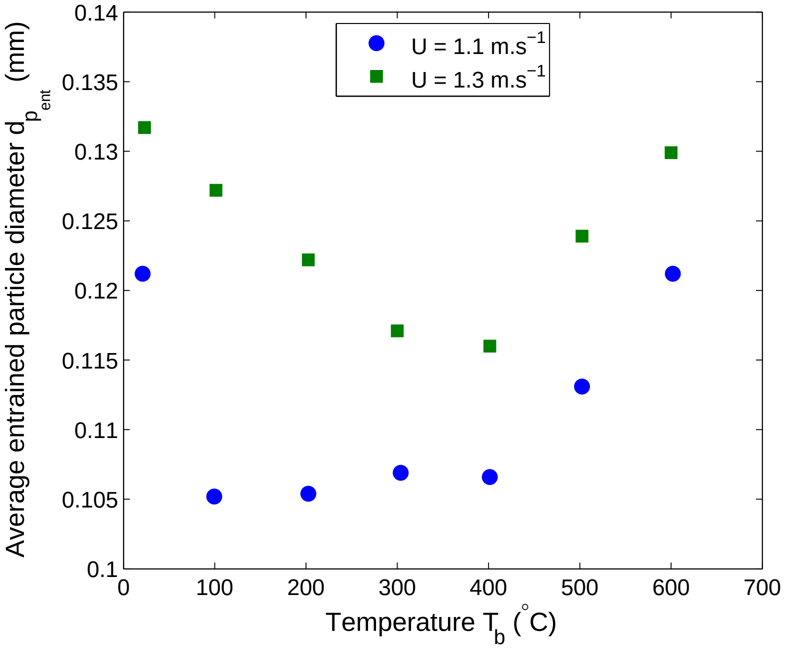

Figure 2.11: Temperature effects on the average diameter for entrained sand particles. From Choi et al. (1998)

for calculating diameters. A summary of the most popular methods follows (Yang, 2003: p.2).

- Sieve diameter – Particles are classified by throwing them through a number of stacked sieves. The particles are then classified according to the smallest aperture size of the square sieve grid through which it will pass.
- Volume diameter – The volume diameter is defined as the diameter of a sphere having the same volume as that of the particle. This can be calculated as:

$$d_v = \left(\frac{6V_p}{\pi}\right)^{\frac{1}{3}} \tag{2.2}$$

- Surface diameter – The surface diameter is defined as the diameter of a sphere having the same surface area as that of the particle. This can be calculated as:

$$d_s = \left(\frac{S_p}{\pi}\right)^{\frac{1}{2}} \tag{2.3}$$

- Surface-Volume diameter – The surface-volume diameter, also known as the Sauter diameter, is defined as a sphere with the same surface to volume ratio as the particle. This can be calculated as:

$$d_{sv} = \frac{6V_p}{S_p} \tag{2.4}$$

- The free-falling diameter – The diameter of a sphere that has the same terminal velocity as that of the particle. If this velocity is in the Stokes law region, the free falling diameter is equal to the Stokes diameter, which can be calculated as

$$d_{st} = \sqrt{\frac{18\mu U_t}{\left(\rho_s - \rho_f\right) g}} \tag{2.5}$$

This effect of the particle diameter can be understood when the traditional force balance on the particle is considered:

$$U_t = \sqrt{\frac{4gd_v\left(\rho_s - \rho_f\right)}{3\rho_f C_d}} \tag{2.6}$$

In equation 2.6 the relationship between the terminal velocity, U_t, and the particle volume diameter, d_v, can be seen. Therefore, even with a constant drag coefficient, C_d, the terminal velocity for a single particle should decrease as the particle diameter decreases. The drag coefficient is typically indirectly proportional to the particle diameter, which makes the terminal velocity an even stronger function of the particle diameter. Therefore, for a smaller diameter particle, a lower terminal velocity is expected. As the terminal velocity decreases, the entrainment flux will increase as well as the elutriation rate from the fluidised bed. Various experimental results show that the elutriation rate constant increases as the particle diameter decreases (Tasirin & Geldart, 1998). This is the expected trend. The trend does deviate from what is expected however, when the particle diameter decreases beyond a certain value. These deviations have been found by many investigators, such as Baeyens et al. (1992), Ma & Kato (1998), Santana et al. (1999) and Smolders & Bayens (1997). Some of the published experimental results can be viewed in figures 2.12 and 2.13. These results have been attributed to the particle interactions. As the particle diameter decreases, the attraction forces between the particles increase. If the particle diameter is decreased sufficiently this attraction forces between the particles increase to such a large extent, that the adhesion forces are larger than the gravitational forces. This causes the particles to clump together in clusters. These clusters act as single large particles, which explains the decrease in the elutriation rate constant.

The critical particle diameter where the elutriation rate constant remains constant, or start to decrease can be calculated by the method suggested by Baeyens et al. (1992)

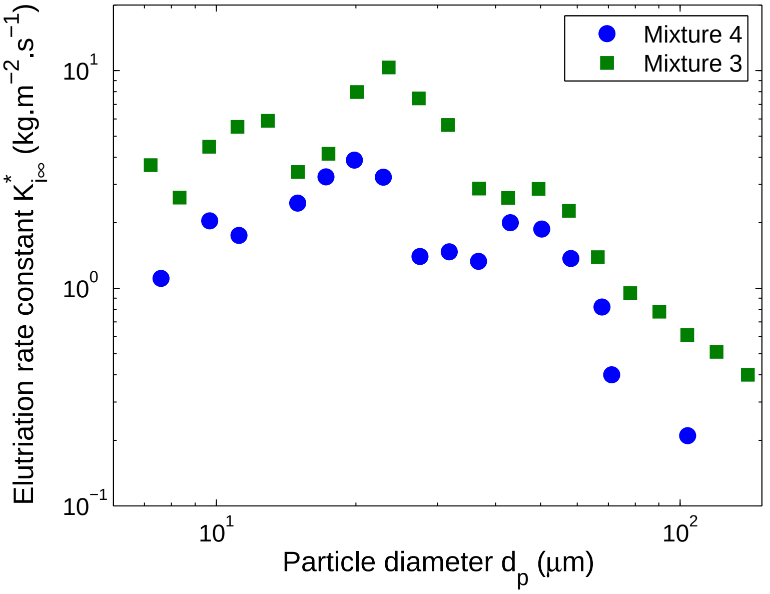

Figure 2.12: Elutriation rate constant as a function of average particle diameter. From Baeyens et al. (1992)

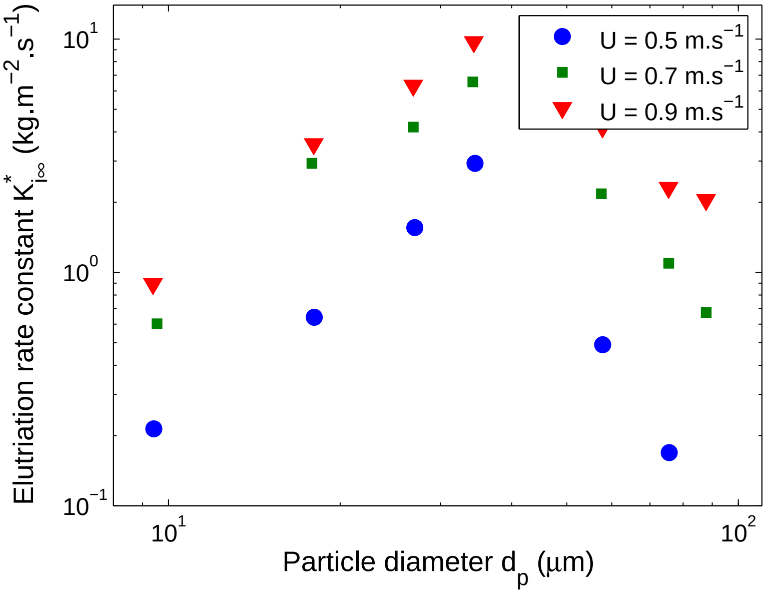

Figure 2.13: Elutriation rate constant as a function of average particle diameter. From Ma & Kato (1998)

as:

$$d_{p_{crit}} {\rho_s}^{0.725} = 1.0325 \times 10^{-2} \tag{2.7}$$

Note that all parameters are in SI units.

Ma & Kato (1998) used a critical cohesion number to calculate the critical particle diameter. The cohesion number uses a cohesion constant, based on the work of Rietema (1984) where the conditions for the cohesion constant were given that, $d_p < 100\,\mu\text{m}$ and $\mu \approx 2 \times 10^{-5}\,\text{Pa.s}$. The critical cohesion number can be seen in equation 2.8.

$$N^*_{coh} = \frac{0.455\rho_s^{0.269}}{\rho_s d_{p_{crit}} g} = 4.5 \tag{2.8}$$

Both the studies of Ma & Kato (1998) and Baeyens et al. (1992) were done with air as fluid, which puts the fluid viscosity in the ballpark given by Rietema (1984). Care should therefore be taken when using a fluid other than air to calculate the critical particle diameter.

Effect of particle shape

The whole operational basis of a fluidised bed rests on the principle that the drag of a fluid on a bed of particles can overcome the weight of these particles. This means that the flow rate of the fluid should at the very least be more than the terminal velocity of the particles. The effect of fines have been discussed in sections 2.2.2 and 2.3.3 as to how they can 'carry' heavier particles out of the freeboard, while clusters of fines can also remain in the freeboard even though the flow rate of the fluid is significantly higher than the terminal velocity of these fines. The consequence of this is that the terminal velocity of a single particle may not always be as indicative of the probability that the particle might be entrained as expected, but the fact remains, terminal velocity does play a role, be it of a individual particle, or of a cluster of particles. One of the major parameters used to calculate the terminal velocity of a particle is the drag coefficient, C_d.

$$C_d = \frac{F}{0.5\rho_f {U_r}^2 A_p} \tag{2.9}$$

The drag coefficient is defined as the ratio of the force on the particle (F), and the fluid dynamic pressure caused by the fluid times the projected area of the particle shown in equation 2.9. The drag coefficient is a 'constant' used to relate the drag force on a particle to the relative velocity of that particle in a fluid and the properties of the fluid. However, the 'constant' called the drag coefficient is not constant. The drag coefficient is only a function of the particle's Reynolds number providing that the fluid is Newtonian (Yang, 2003: p.15). This means that the drag coefficient is a function of the same properties it is used with to calculate the drag force. The diameter used to calculate the Reynolds number however is the diameter associated with the projected area of the particle. The drag coefficient is therefore affected by the shape of the particle, which in turn affects the terminal velocity of the particle. Equations have been developed to calculate the drag coefficients for non-spherical particles, but these correlations are mostly for axisymmetric particles such as spheroids, cylinders and other regular particles. No proper correlation have been developed for the prediction of drag over arbitrarily shaped particles (Yang, 2003: p.17). However, some correlation has to be used, as something is better than nothing. The correlation for the drag coefficient developed by Haider & Levenspiel (1989) as seen in equation 2.10 will be used in this study.

$$C_d = \begin{array}{l} \frac{24}{\mathrm{Re}_p}\left[1 + \left(8.1716 \times \exp\left(-4.0655\Psi\right)\right)\mathrm{Re}_p^{0.0964+0.5565\Psi}\right] \\ + \frac{73.69(\exp(-5.0748\Psi))\mathrm{Re}_p}{\mathrm{Re}_p + 5.378\times\exp(6.2122\Psi)} \end{array} \tag{2.10}$$

The terminal velocity of a particle is a function of the linear velocity of that particle, accounted for with the term Re_p in equation 2.10. The sphericity (Ψ) of a particle should influence the terminal velocity, by reducing the terminal velocity as the sphericity of the particle is decreased. If equation 2.10 is used to calculate the drag coefficient as a function of the sphericity, the effect of sphericity on the terminal velocity can be seen in figure 2.14.

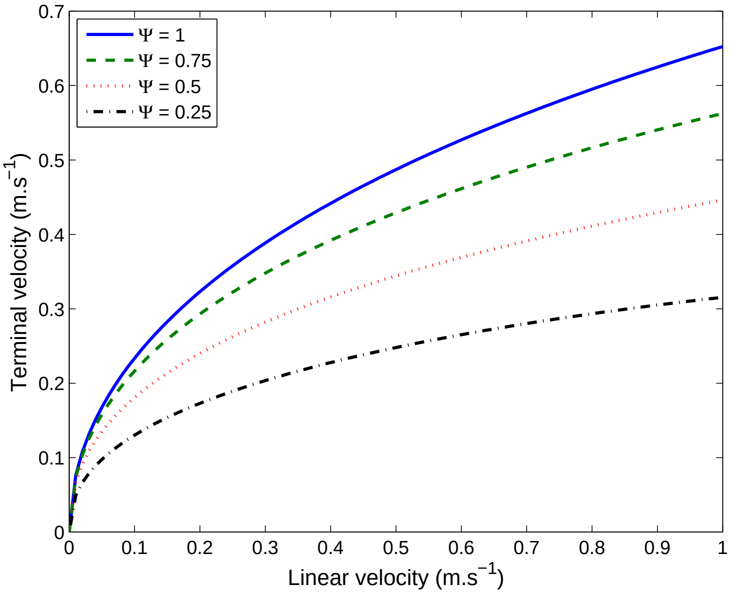

Figure 2.14: The effect the linear velocity and sphericity of a particle has on the terminal velocity of the same particle

Sphericity

Sphericity, Ψ, is the most common method used to quantify the shape of particles. A sphere is the shape in which the surface area exposed is minimised with a given amount of volume. A particle with a large surface area with respect to the volume will therefore be less spherical. This concept is used to define the sphericity of a particle. Wadell (1933) suggested a 'degree of true sphericity' which can be calculated as:

$$\Psi = \frac{\pi^{\frac{1}{3}} \left(6V_p\right)^{\frac{2}{3}}}{A_p} \tag{2.11}$$

True sphericity can be difficult to measure directly as the measurement of irregular particle surfaces can be rather involved. For this reason Wadell (1933) suggested the use of an 'operational' sphericity which can be calculated as

$$\Psi_{op} = \left(\frac{\text{Volume of particle}}{\text{Volume of smallest circumscribing sphere}}\right)^{\frac{1}{3}} \tag{2.12}$$

For spheroids or relatively rounded particles the operational sphericity can be calculated as

$$\Psi_{op} = \left(e_1 e_2\right)^{-\frac{1}{3}} \tag{2.13}$$

where e_1 and e_2 are the flatness and elongation ratio respectively. They can be calculated by:

$$e_1 = \frac{b}{t} \tag{2.14}$$

$$e_2 = \frac{l}{b} \tag{2.15}$$

The thickness, t, is calculated as the minimum distance between two tangential surfaces, where one of these surfaces are the plane of maximum stability for the particle. The breadth, b, is defined as the minimum distance between two tangential surfaces that are perpendicular to the surfaces used to measure the thickness. The length, l, can be calculated from a surface that lies normal to the surfaces used in the thickness and breadth measurements. Note that the size of these particle characteristics should follow the relationship, $t < b < l$.

When using any other arbitrary particle shape than spheroids it is understandable that Ψ_{op} will not be a good approximation for the true sphericity. Aschenbrenner (1956) suggested the use of a working sphericity rather then the operational sphericity. The working sphericity has been reported to work sufficiently for predicting the settling behaviour of naturally occurring mineral particles. The working sphericity can be calculated as

$$\Psi_w = \frac{12.8\left(e_1 e_2{}^2\right)^{\frac{1}{3}}}{1 + e_2\left(1 + e_1\right) + 6\sqrt{1 + e_2{}^2\left(1 + e_1{}^2\right)}} \tag{2.16}$$

Although Wadell (1934) claimed that the sphericity can be used to correlate the drag coefficient of a particle, Isaacs & Thodos (1967) reported that sphericity is inadequate to describe drag flow even over smooth cylinders, not to mention irregular particles. Sphericity has its uses such as to adjust for the particle diameter when working inside a packed bed, or when a correlating parameter is necessary to describe creeping flow past bodies that geometrically resemble spheres. But sphericity as a shape descriptor is lacking when correlating particle drag for irregular particles (Thompson & Clark, 1991). Despite the fact that the sphericity has these known drawbacks, it is a well known and well understood shape descriptor, which would explain its popularity in elutriation rate constant correlations.

Other particle shape descriptors

Circularity is for two dimensions what sphericity is for three dimensions. It is defined as the ratio of the circumference of a sphere with the same cross-sectional area as the particle cross section and the actual circumference of the particle cross section:

$$\mathsf{C} = \frac{\pi d_{eq}}{\text{Particle circumference}} \tag{2.17}$$

As can be seen from equation 2.17 the circularity of a particle should be calculated from a two dimensional projection of a particle. This method is normally used in conjunction with image processing, where a two dimensional photo of particles is obtained, either with a camera or with a microscope, depending on the resolution required and the size of the particles. The method with which the circularity of a particle is calculated makes it a much easier method to use as a shape descriptor because it does not involve the measurement of the entire surface area of the particle. Smolders & Bayens (1997) used a circularity obtained from a microscope instead of a sphericity to calculate particle terminal velocities.

A full review of the popular shape description techniques can be seen in appendix A. These techniques include Heywood shape factors, Fourier descriptors, Fractal dimensions, Polygonal harmonics, Piper's angle and Delta analysis and Multi-scale roughness descriptors. Of these techniques, the fractal dimensions, polygonal harmonics and Piper's angles, together with the circularity will be applied in this study to attempt to differentiate between particle shapes.

In a study on liquid–solid fluidisation Flemmer et al. (1993) did a review on how particle shape can influence the hydrodynamics of a single particle. It was found that no well-accepted correlation exists that includes the effect of particle shape on hydrodynamics for even single irregular particles, not to even mention mixtures of particles as found in fluidised beds. In the study mentioned, Flemmer et al. (1993) went ahead to study the modern techniques of particle shape description and how they might be used to adjust for the effect of shape in fluidisation behaviour. The voidage during homogeneous fluidisation was chosen as the parameter to test the effect of shape on. Although the conclusions drawn can not be applied on a gas–solid fluidised bed, It does give a good starting point for a study on the effect of particle shape on gas–solid fluidisation. Sookai et al. (2005) did a study on different particle shapes, sizes and densities in gas–solid fluidisation. They found that particles with a high sphericity tend to entrain more readily than particles with a low sphericity.

2.4 Modelling Entrainment and Elutriation

2.4.1 Entrainment flux

As stated previously, for particles to be transported into the freeboard and to be entrained by the gas flowing out of the fluidised bed, they first have to be ejected into the freeboard from the bed surface. The ejection of the particles into the freeboard is a complex process (As all fluidised bed processes) of clusters, strands and single particles all accelerating, decelerating, colliding with each other, separating from each other, etc. To be able to describe this complex process, simplifying assumptions have been made to reduce the process to three phases, or two entrainment flows. Both of these assumptions are reputed to lead to similar results (Yang, 2003: p.124). But as the two phase description is easier to understand, it will be explained here.

In short the entrainment flux flowing from the fluidised bed surface to the fluid outlet can be divided into two streams – One stream of solids that are entrained and will flow all the way to the fluid outlet to leave the bed and one stream of solids decreasing in velocity until they fall back to the bed. This can be described as:

$$E_{i_h} = E_{i\infty} + E_{i0}\exp\left(-a_i\, h\right) = x_{B_i} K^*_{i\infty} + E_{i0}\exp\left(-a_i\, h\right) \tag{2.18}$$

Therefore to calculate a value for the entrainment flux at a height between the bed surface and the TDH, it is necessary to know the elutriation rate constant, $K^*_{i\infty}$, the entrainment flux at the bed surface, E_{i0}, and the exponential decay coefficient, a_i. Wen & Chen (1982) stated that a_i varies between 3.5 and $6.4\,\mathrm{m}^{-1}$. A value of $4\,\mathrm{m}^{-1}$ is recommended in cases where little information is known about the system. Note that equation 2.18 reduces to elutriation rate constant at a height, h, equal to or higher than the TDH.

The entrainment flux at the bed surface can be calculated from having entrainment fluxes at two different heights. Alternatively, one of the correlations in table 2.1 can be used.

Table 2.1: Commonly used correlations to predict the entrainment flux at the fluidised bed surface, E_0

No	Correlation	Reference
1	$E_0 = 3.07 \times 10^{-9} \frac{A d_b \left(U - U_{mf}\right)^{0.25} \rho_g^{3.5} g^{0.5}}{\mu^{2.5}}$	Wen & Chen (1982)
2a	Bubble nose model $E_0 = 3 d_p \frac{\left(1 - \epsilon_{mf}\right)\left(U - U_{mf}\right)}{d_b}$	Pemberton & Davidson (1986)
2b	Bubble wake model $E_0 = 0.1 \, \rho_s \left(1 - \epsilon_{mf}\right)\left(U - U_{mf}\right)$	Pemberton & Davidson (1986)
3	$E_0 = 9.6 \, \left(U - U_{mf}\right) A \, d_b \, \left(\frac{298}{T_b}\right)^{3.5}$	Choi et al. (1989)

2.4.2 Elutriation rate constant

The elutriation rate constant, K_{ih}^*, is defined as the ratio of the instantaneous rate of solid removal of the particle size, d_{p_i}, per unit cross sectional bed area, A, to the fraction of the mass of bed material, X_{B_i}, with the particle size, d_{p_i} (Yang, 2003: p.116). This can be expressed mathematically as:

$$K_{ih}^* = \frac{E_{ih}(t)}{x_{B_i}(t)} \tag{2.19}$$

with the entrainment flux, E_{ih}, defined as:

$$E_{ih}(t) = \frac{1}{A} \frac{d}{dt} \left(x_{B_i}(t) M_B(t)\right) \tag{2.20}$$

The elutriation rate constant is normally determined in batch experiments. To do this the mass of solids captured over a time, t, have to be correlated with the elutriation rate constant. This can be done by integrating equation 2.20. This will result in:

$$M_{i_t} = x_{B_i0} \, M_B \left[1 - \exp\left(-\frac{K_{ih}^* \, A}{M_B}\right)\right] \tag{2.21}$$

Note that the integration of equation 2.20 is only accurate when the mass of solids in the bed, M_B, does not change much with respect to time. The exponentially decreasing concentration profile of solids in the freeboard is a well known occurrence (Kunii & Levenspiel, 1991: p.177). Care should be taken therefore to know exactly what elutriation is measured. If the elutriation is measured at a height below the Transport Disengagement Height (TDH), it cannot be compared with the elutriation rate constant, $K^*_{i\infty}$ given by most correlations.

The method by which elutriation is measured together with equation 2.18 explains why the terms elutriation and entrainment are so often interchanged in literature. An elutriation rate constant is used to predict an entrainment flux above the TDH. Therefore, above the TDH, the elutriation rate and the entrainment flux is equal when doing a batch experiment. This is because in a batch experiment all the entrained solids are removed from the fluidised bed and can therefore be considered as elutriated solids. This fact should be noted to ensure that one does not get confused by the interchangeability of these terms in literature.

The elutriation rate constant is one of the parameters in fluidised beds that has the most correlations to predict it, as it is so hard to determine from first principles due to the complex and chaotic nature of the fluidised bed freeboard. A list of the most widely used correlations can be seen in table 2.2. The earliest commonly used correlation is the one determined by Zenz & Weil (1958). They considered the freeboard above the TDH to behave like a pneumatic transport line at choking conditions. What this means is that the freeboard above the TDH carries as much solids as is possible, before the solids start to influence each other and start to increase the effective particle diameter. This choking specification is commonly used in the description of pneumatic transport lines. The entrainment flux above the TDH can therefore be calculated by dividing the bed contents into a number of particle diameters, and calculating the choking load for each of these diameters. The entrainment flux for each diameter can be calculated as:

$$E_{i\infty} = x_{B_i} G_{s_i} \tag{2.22}$$

With the entrainment flux for each particle diameter known, the total flux can be calculated by adding all the fluxes together.

This method for calculating the total elutriation rate constant is most commonly used in elutriation rate constant correlations, as can be seen in equations 2, 3, 4, 5, 6, 7, 10 and 11 in table 2.2. The biggest difference in the various correlations is the way in which the choking loads and the particle size distributions are calculated (Yang, 2003).

Table 2.2: Commonly used correlations for the Elutriation rate constant $K^*_{i\infty}$

No	Correlation	U (m/s)	D (m)	d$_p$ (μm)	Reference
1	$\frac{K^*_{i\infty}\, g\, d^2_{p_i}}{\mu (U-U_t)^2} = 0.0015\, \mathrm{Re}_t^{0.6} + 0.01\, \mathrm{Re}_t^{1.2}$	0.3 - 1.0	0.07 - 1.0	100 - 1600	Yagi & Aochi (1955) as quoted by Lin et al. (1980)
2	$\frac{K^*_{i\infty}}{\rho_f\, U} = \begin{cases} 1.26 \times 10^7 \left(\frac{U^2}{g\, d_{p_i}\, \rho_s^2}\right)^{1.88} & \text{for } \frac{U^2}{g\, d_{p_i}\, \rho_s^2} < 3.1 \\ 1.31 \times 10^4 \left(\frac{U^2}{g\, d_{p_i}\, \rho_s^2}\right)^{1.18} & \text{for } \frac{U^2}{g\, d_{p_i}\, \rho_s^2} > 3.1 \end{cases}$	0.3 - 0.7	0.05 × 0.53	40 - 200	Zenz & Weil (1958)
3	$\frac{K^*_{i\infty}}{\rho_f \left(U-U_{t_i}\right)} = 1.52 \times 10^{-5} \left(\frac{\left(U-U_{t_i}\right)^2}{g\, d_{p_i}}\right)^{0.5} Re^{0.725}$	0.6 - 1.0	0.102	700	Wen & Hashinger (1960)
4	$\frac{K^*_{i\infty}}{\rho_f \left(U-U_{t_i}\right)} = 4.6 \times 10^{-2} \left(\frac{\left(U-U_{t_i}\right)^2}{g\, d_{p_i}}\right)^{0.5} Re^{0.3} \left(\frac{\rho_s-\rho_f}{\rho_f}\right)^{0.15}$	0.9 - 2.8	0.031 - 0.067	700 - 1900	Tanaka et al. (1972)
5	$\frac{K^*_{i\infty}}{\rho_f\, U} = B + 130 \exp\left[-10.4 \left(\frac{U_{t_i}}{U}\right)^{0.5} \left(\frac{U_{mf}}{U-U_{mf}}\right)^{0.25}\right]$ with B $= 10^{-4}$ to 10^{-3}	0.6 - 2.4	0.91 × 0.91	60 - 1000	Merrick & Highley (1974)
6	$\frac{K^*_{i\infty}}{\rho_f\, U} = 23.7 \exp\left(-5.4 \frac{U_{t_i}}{U}\right)$	0.6 - 3.0	0.076	60 - 220	Geldart et al. (1979)

Continued on Next Page . . .

No	Correlation	U ($^{m}/_{s}$)	D (m)	d$_p$ (μm)	Reference
7	$\frac{K^*_{i\infty}}{\rho_f\,U} = 9.43 \times 10^{-4}\left(\frac{U^2}{g\,d_p}\right)^{1.65}$ $58 \leq \left(\frac{U^2}{g\,d_p}\right) \leq 1000$ $0 < d_p < 74\mu m$	0.1 - 0.3	0.61 × 0.61	10 - 125	Lin et al. (1980)
8	$K^*_{i\infty} = 0.011\,\rho_s\left(1 - \frac{U_{t_i}}{U}\right)^2$	0.9 - 3.7	0.92 × 0.92	300 - 1000	Colakyan & Levenspiel (1984)
9	$K^*_{i\infty} = 2.8 \times 10^{-2}\left(\frac{U-U_{t_i}}{U}\right)^{1.6}\left(\frac{\rho_s-\rho_f}{\rho_s}\right)^{0.54\,U_{t_i}^{2.1}} D_h$				Kato et al. (1985: p. 134 -147) as quoted by Yang (2003)
10	$\frac{K^*_{i\infty}}{\rho_f\,U} = 2.908\left(\frac{U^2}{g\,d_p}\right)^3\left(\frac{\rho_f}{\rho_s}\right)^2\left(\frac{g\,d_p}{g\,d_b}\right)^3$				Subbarao (1986)
11	$\frac{K^*_{i\infty}}{\rho_f\,U} = 1.6\left(\frac{U}{U_{t_i}}\right)\left(1 - \frac{U_{t_i}}{U}\right)$				Ściążko et al. (1991)
12	$K^*_{i\infty} = 5.4 \times 10^{-5}\rho_s\left(\frac{U}{0.2}\right)^{3.4}\left(1 - \frac{U_{t_i}}{U}\right)^2$ for $d_p \leq \frac{1.0325\times 10^{-2}}{\rho_s^{0.725}}$	0.2 - 0.7		30 - 780	Baeyens et al. (1992)
13	$K^*_{i\infty} = 0.35\,\rho_s U A\,(1-\epsilon)_H$ with $(1-\epsilon)_H = 7.41 \times 10^{-3} R^{1.87} A^{0.55} H_F^{-0.64} B$ and $R = \Sigma x_i\left(\frac{U-U_{t_i}}{U_{t_i}}\right)$ for $U_{t_i} < U$	0.1 - 0.6	0.071 0.08 × 0.08 0.15 × 0.15	30 - 200	Nakagawa et al. (1994)

Continued on Next Page . . .

No	Correlation	U ($^{\mathrm{m}}/_{\mathrm{s}}$)	D (m)	d$_p$ (μm)	Reference
14	$K^*_{i\infty} = \begin{cases} 23.7\rho_f U^{2.5}\exp\left(-5.4\frac{U_{t_i}}{U}\right) & \text{for } \mathrm{Re}_c < 3000 \\ 14.5\rho_f U^{2.5}\exp\left(-5.4\frac{U_{t_i}}{U}\right) & \text{for } \mathrm{Re}_c > 3000 \end{cases}$	0.2 - 0.8	0.076 and 0.152	17 - 77	Tasirin & Geldart (1998)
15	$\frac{K^*_{i\infty} d_p}{\mu} = \mathrm{Ga}^{0.5}\exp\left(6.92 - 2.11F_g^{0.303} - \frac{13.1}{F_d^{0.902}}\right)$ with $F_g = g\,d_p\,(\rho_s - \rho_f)$ $F_d = C_d\frac{\rho_f U^2}{2}$	0.3 - 0.7	0.06 - 1.1	50 - 1000	Choi et al. (1999)

Another commonly used assumption is to calculate the flux of solids from the dense bed into the freeboard by using bubble properties, such as size, velocity, etc. This method has been used by Smolders & Bayens (1997) and George & Grace (1978) as quoted by Yang (2003). The problem with this method is that it is assumed that the flux above the TDH is only that of the particles with a terminal velocity less than the fluid velocity in the freeboard. This is known to be inaccurate from experimental investigations, as stated in section 2.2.2.

Most of the other correlations (Equations 1, 8, 9, 12, 13, 14 and 15 in table 2.2) for the elutriation rate constant are empirically fitted models with little or no theoretical basis.

When any of the correlations listed in table 2.2 are used, care should be taken so that the correlation is chosen for a system similar to that on which the correlation was developed, as these correlations can differ significantly. This significant difference can be seen in figure 2.15. Note that most of the correlations predict values within a factor 100 of each other. But some of the correlations differ more than a factor 10^6.

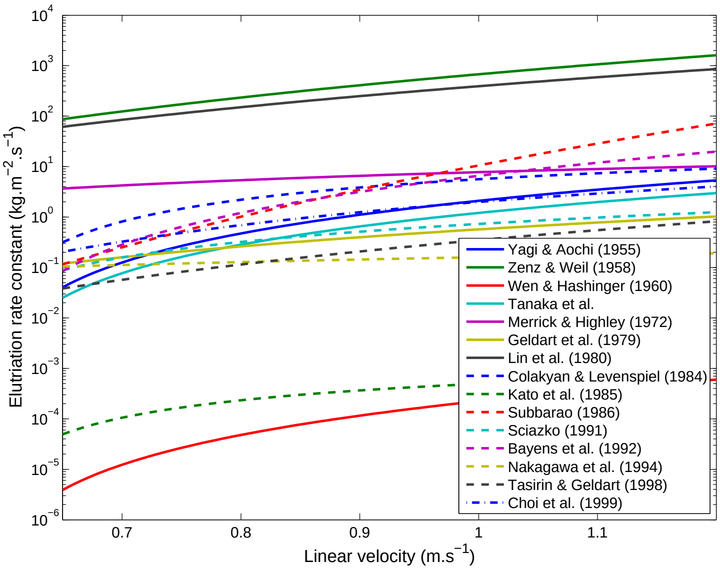

Figure 2.15: Comparison between the different correlations for the elutriation rate constant $K^*_{i\infty}$ (Numbers in legend refers to correlation number as used in table 2.2)

To better understand these correlations and when necessary, make small modification to these correlations to better fit a specific system, the principles, or pseudo-principles behind these equations has to be understood properly. Dimensionless groups are mostly used as dimensional analysis makes it easier to develop empirical correlations. Even though the dimensionless groups can be completely meaningless in some cases, most of the time the groups have some physical representation which is associated with the entrainment process. These groups are:

- $K^*_{i\infty}/\rho_f U$, used in all of the correlations based on the pneumatic transport line method, is the ratio of the solids mass flux and the gas mass flux
- U^2/gd_p, also known as the Froude number (Fr), is the ratio between the inertial force on the particles and the gravity force on the particle
- $U - U_{t_i}$ can be used in place of the superficial velocity U. This is known as the slip velocity which is a direct indication of how much higher the superficial velocity is than the terminal velocity for a specific particle size. It is therefore a measure of how quickly a particle can be removed from the freeboard. The problem with using a slip velocity is that the slip velocity implies that only particles with a terminal velocity below the superficial velocity of the gas in the freeboard are entrained, which have been proved incorrect as mentioned in section 2.2.2
- U_{t_i}/U is another way to represent the slip velocity that allows for particles with a terminal velocity higher than the freeboard superficial velocity to be entrained
- The Reynolds number (Re_p) is also used in some correlations as an additional velocity term together with the slip velocity and the Froude number
- ρ_f/ρ_s or $\rho_s - \rho_f/\rho_f$ is a density ratio, which is used to adjust for the density effects such as a denser gas, or heavier particles.

As figure 2.14 indicated, the terminal velocity of a particle is decreased when the sphericity is reduced. This implies that less spherical particles should have a higher entrainment rate if the hydrodynamics can be described by the behaviour of a single particle. Figure 2.16 shows how some of the correlations in table 2.2 quantifies the effect of particle shape on entrainment rate for similar sized particles. According to these models, particle shape should therefore have an effect on the entrainment rate. However, no study has been found in literature where all the particle properties, except for particle shape, has been kept constant to verify whether any of the models are applicable to include the effect of particle shape, and more importantly is it sufficient to only adjust the coefficient of drag for a single particle with a sphericity to include the effect of particle shape on entrainment.

2.5 Concluding remarks

Entrainment is a well known occurrence in fluidised beds and in many cases, entrainment is considered to be problematic, as the loss of solids from the bed is responsible for additional costs. The process of entrainment is still not very well understood and many of the factors that influence entrainment are correlated empirically instead of phenomenologically or fundamentally. Important factors are therefore lumped in empirical constants

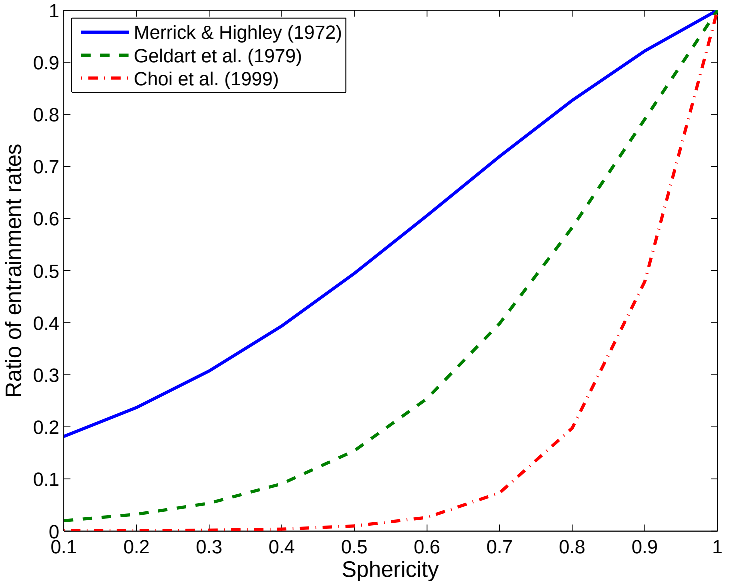

Figure 2.16: The ratio of entrainment rates for different sphericities, where the ratio is defined as: $\frac{\text{Entrainment rate of particles with a sphericity of 1}}{\text{Entrainment rate of particles with a sphericity of the value on the x-axis}}$

from time to time, which would explain why there is such a large deviation in the values predicted for the elutriation rate constants. One factor that is left out in most cases is the shape of the solids. It is true that the shape of the solids is taken into consideration when calculating the terminal velocity of the solids, but when studying the literature on elutriation rate constant correlations, little information is given on how a sphericity, if at all, was determined. The purpose of this study is to evaluate how shape can influence the entrainment rate of solids and to see how different shape characterisation techniques report different shape factors. This will be done by using two particle mixtures with identical properties except for the particle shapes in entrainment tests. There is also a shortage of information in literature on how heavier particles behave in fluidisation. This study is aimed at helping to understand the entrainment behaviour in high temperature Fischer-Tropsch (HTFT) reactors better. These reactors use an iron based catalyst, which is exactly the type of solid on which fluidisation behaviour is scarce.

CHAPTER 3

Experimental

3.1 Experimental Setup

3.1.1 Materials

The solid packing used in the fluidised bed was Ferrosilicon (FeSi) obtained from BHP-Billiton. Two types of FeSi were used, atomised FeSi and milled FeSi. Both the atomised and the milled FeSi are non-porous. A mixture of 50% atomised and 50% milled FeSi by mass was also used. A description of these solids can be seen in table 3.1. A sample of how the atomised and the milled FeSi differ in appearance can be seen in figure 3.1. The FeSi was chosen as the solid to be fluidised since the FeSi is very similar in physical

Table 3.1: Properties of particle mixtures used inside fluidised bed reactor

Property	Atomised FeSi	Milled FeSi	Mixture
Volume weighted mean particle diameter	38.44 μm	49.96 μm	41.78 μm
Solid density	6690 $\mathrm{kg/m^3}$	6589 $\mathrm{kg/m^3}$	6621 $\mathrm{kg/m^3}$
Solid packing density	3753 $\mathrm{kg/m^3}$	3490 $\mathrm{kg/m^3}$	3630 $\mathrm{kg/m^3}$
Geldart classification	A-B	A-B	A-B
Particle shape	Spherical	Irregular	Both irregular and spherical

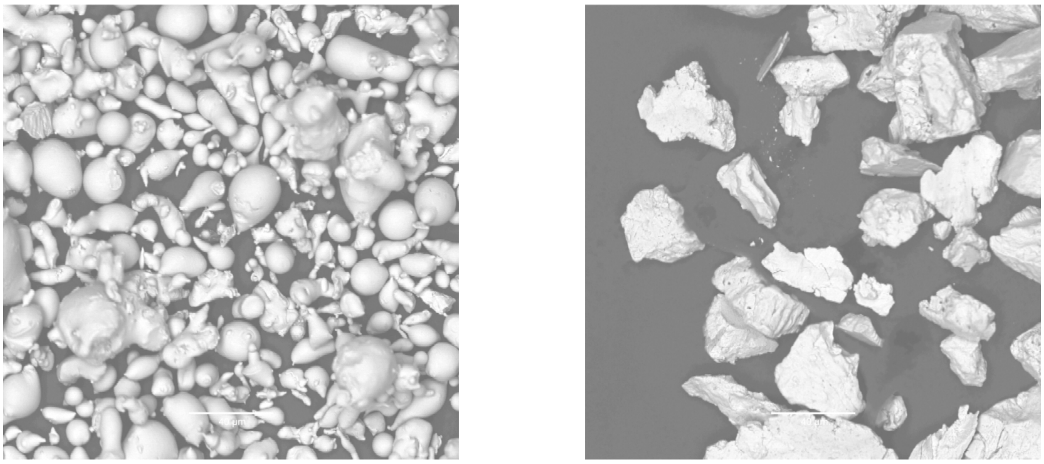

(a) A scanning electron microscope image of the atomised FeSi

(b) A scanning electron microscope image of the milled FeSi

Figure 3.1: A comparison of the difference in appearance between the atomised and the milled FeSi

properties to the high temperature Fischer-Tropsch (HTFT) catalyst. Both the FeSi and the HTFT catalyst lies on the Geldart A-B boundary, which causes the solids to have both Geldart A and Geldart B behaviour.

The densities of the FeSi mixtures were determined by measuring the displacement of water by a certain mass of solids. Care was taken to ensure that only the solids are responsible for displacing the water and that no air bubbles were trapped along with the solids. The packing densities of the mixtures were determined for a tightly packed mixture, as this was the state in which the solids were found in the dipleg where the entrainment measurements were made.

3.1.2 Equipment

All tests were done in a 140 mm perspex column, with a height of 5.5 m. A schematic diagram of this experimental setup can be seen in figure 3.2. Air, supplied by a BSC15 Evolution Fini Compressor (SC-1 in the diagram), was used as the fluidising medium. The flow rates to the fluidised bed and the cyclone were measured by the flow meters FT-2 and FT-1 respectively, which were both HO11/4X11/4-20-CB-1MC3PA-NTP-X Hoffer turbine flow meters. These flow meters are reported to have an accuracy of 0.25% and are able to measure flow rates of 5 to 100 actual cubic meters per hour with a 1% linearity, which means that a high level of precision can be expected. The pressure drop was measured over various sections of the setup with Rosemount 3051 differential pressure transmitters. The detail for each transmitter can be seen in table 3.2. All of the above mentioned instrumentation has 4 - 20 mA analog output signals, which were recorded on a Datataker DT500 series 3. The data of all the instrumentation could then be extracted

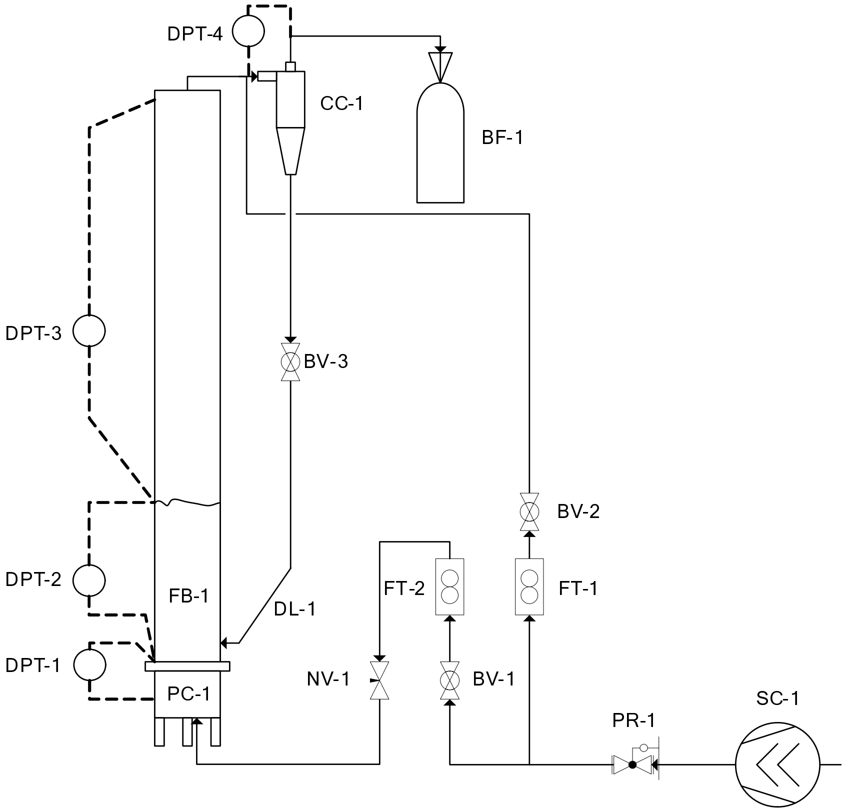

FB-1 : Fluidised bed
PC-1 : Plenum chamber
SC-1 : Compressor
CC-1 : Cyclone
BF-1 : Bag Filter
DL-1 : Dip leg for solids return
DPT-1 : Differential pressure cell
DPT-2 : Differential pressure cell
DPT-3 : Differential pressure cell
DPT-4 : Differential pressure cell
PR-1 : Pressure regulator
FT-1 : Turbine flow meter
FT-2 : Turbine flow meter
BV-1 : Ball valve
BV-2 : Ball valve
BV-3 : Ball valve
NV-1 : Needle valve

Figure 3.2: A schematic of the experimental setup used for all the tests

from the Datataker into a spreadsheet.

A chiller was used to maintain the air temperature at 15 °C at all times, while the pressure regulator, PR-1 as seen in figure 3.2, was used to maintain the fluidised bed pressure at 15 kPag. With temperature and pressure constant, as well as all the other factors verified, it is possible to measure only the effect of particle shape on entrainment rate.

3.2 Method

The fluidised bed is a chaotic system and small disturbances can therefore cause a major deviation in the operating point of the bed. It is therefore important to ensure that the values are measured under the same conditions.

Prior to every set of experiments, the bed was packed with about 30 kg of FeSi. This

Table 3.2: Detail information of differential pressure drop transmitters

Label in figure 3.2	Range	Accuracy	Function
DPT-1	0 - 63 kPa	0.1%	Measure gas distributor pressure drop
DPT-2	0 - 63 kPa	0.1%	Measure dense bed pressure drop
DPT-3	0 - 63 kPa	0.1%	Measure freeboard pressure drop
DPT-4	0 - 63 kPa	0.1%	Measure cyclone pressure drop

was done to ensure that even at the highest entrainment rate, the loss of solids from the bed will be less than 20% of the total bed mass, as suggested by Kunii & Levenspiel (1991: p.176) for batch experiments.

3.2.1 Minimum fluidisation measurements

The minimum fluidisation velocity of a fluidised bed should give an indication of what the morphology of the bed is like. How the particles pack together in a fluidised bed will be affected by the shape of these particles. To measure the minimum fluidisation velocity, the bed was first fluidised at a higher velocity after which the ball valve, BV-1, was shut quickly to ensure that the bed is in a loosely packed state. All the excess gas in the bed was then allowed to escape over a period of 10 minutes, so to ensure that the true minimum fluidisation velocity is measured. BV-1 was opened again, after the needle valve, NV-1, was closed completely. NV-1 was then opened a small fraction and the pressure drop over the bed was recorded from the differential pressure transmitter, DPT-2. After the pressure drop measured by DPT-2 stabilised to a constant value, NV-1 was opened a fraction more. This process was repeated until the bed started bubbling. The pressure drop profile as a function of the linear velocity can then be used to calculate the minimum fluidisation velocity. This techniques is a common method to measure the minimum fluidisation velocity as can be seen in the work of Chitester et al. (1984) and Adánez & Abanades (1991), where the minimum fluidisation velocity is read off at the inflection point on the pressure drop profile.

3.2.2 Entrainment measurements

Entrainment rates were measured at five different flow rates. A list of the operating conditions of the fluidised bed can be seen in table 3.3. The cooled down air naturally has a low moisture content as a result of the cooling process. The low humidity together

Table 3.3: Operating conditions used for the fluidised bed

Flow rate Condition	0.17 m/s	0.24 m/s	0.32 m/s	0.38 m/s	0.43 m/s
Pressure	102 kPaa	102 kPaa	102 kPaa	102 kPaa	102 kPaa
Temperature	15 °C	15 °C	15 °C	15 °C	15 °C

with the material used for the column, and the type of solids used resulted in a high charge of static electricity forming on the column walls. To counter act this, a copper wire was wound around the column, with special focus on the dipleg in which the solids from the cyclone are returned to the dense bed. This resulted in the column being well earthed which caused less solids sticking to the column side and less static shocks for the masters student. The air to the fluidised bed was opened by opening ball valves, BV-1 and BV-2. Then the needle valve, NV-1, was used to control the air flow rate into the fluidised bed at the specified value. The fluidised bed was then left to reach a steady state to ensure that only the entrainment rate was measured and not the fluidised bed dynamics. Steady state is defined as the point where the solids level in the dip-leg remains constant. When this state is reached, the ball-valve, BV-3, is closed to capture the entrained solids – which under normal conditions are returned from the cyclone via the dip-leg to the bed. The fluidised bed is operated with ball-valve BV-3 closed for a set period of time, after which the air flow into the fluidised bed is stopped by closing ball-valves BV-1 and BV-2. The dip-leg is then tapped to ensure that the packing of the solids inside the dip-leg can always be considered to be in a 'tightly packed' state. This is also the packing state for which the bulk densities of the FeSi was measured. The height of the tightly packed solids above BV-3 is then measured to calculate the mass of solids removed from the bed due to entrainment.

3.2.3 Repeatability

The chaotic nature of the fluidised bed have been mentioned and the effect of this on experimental measurements should be obvious. It is therefore necessary to ensure that the experimental setup has a sufficiently good repeatability. This was done by loading the bed with a batch of solids and measuring the entrainment rate, after which the bed was drained and the following type of solids was loaded and the entrainment was measured. This was done for all three the solid mixtures. After all three solids were tested, the process was repeated again. The repeatability of the experimental setup can be seen in table 3.4. Note that the average values of the entrainment rate for the different particle mixtures are used as the benchmark against which the measured values are checked, as can be seen in equation 3.1.

$$\text{AARE} = \sum_{i}^{n} \frac{|\text{Entrainment rate}_{\text{Average}} - \text{Entrainment rate}_{\text{Measured}}|}{\text{Entrainment rate}_{\text{Average}}} \frac{1}{n} \times 100 \qquad (3.1)$$

When studying these errors, it can be seen that size the experimental error is far from ideal, however, errors, of this size, in the few cases where errors are shown, are frequently found in literature on entrainment data (Merrick & Highley, 1974; Geldart et al., 1979; Lin et al., 1980).

Table 3.4: Relative errors in entrainment for different particle mixtures with respect to the average value of entrainment for the different particle mixtures

Solids mixture	AARE	Maximum
Atomised FeSi	14.28%	40.19%
Milled FeSi	18.72%	32.99%
FeSi Mixture	3.77%	20.12%

3.2.4 Procedure verification

To ensure that particle shape is the only effect being studied, some tests had to be done to verify that the other factors described in chapter 2 are kept constant for all three particle mixtures used.

Particle size distribution

All the information on the size of the particles used was obtained with a Malvern Mastersizer 2000. The Malvern uses laser diffraction to measure the particle size distribution of a sample. The particle size measured by the Malvern is a volume mean diameter.

The particle size has a significant effect on the entrainment rate, as already mentioned in section 2.3.3. For particles below the critical particle diameter, the entrainment rate of that particle size can be assumed to be the same value as that of the critical particle diameter. For FeSi, this critical diameter is ±17 μm. A comparison of the particle size distributions can be seen in figure 3.3. This figure gives a good indication that the all the particle mixtures should behave similarly as a result of the particle diameter. All the mixtures contains a significant fraction of fines, a comparison of the percentage of fines

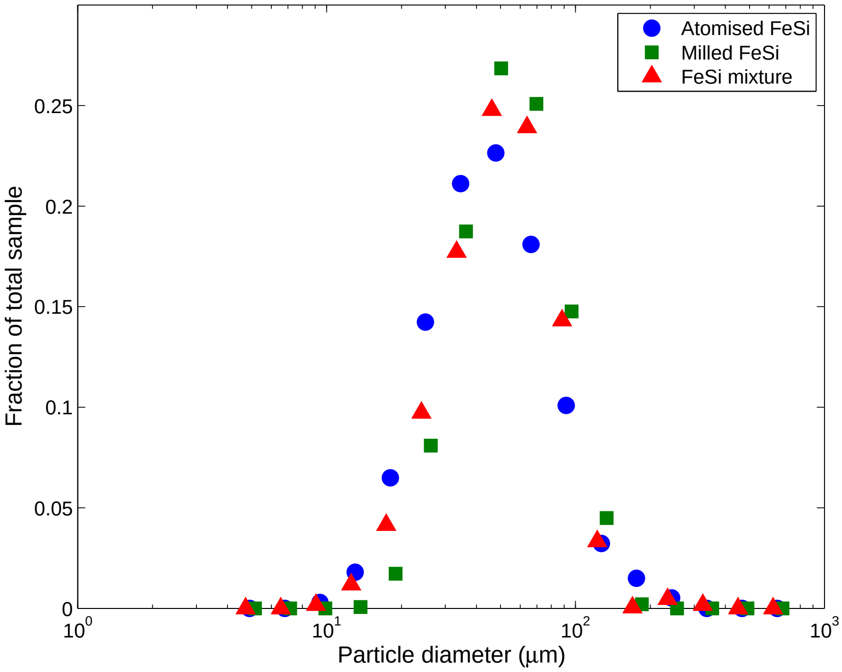

Figure 3.3: A comparison for the particle size distribution for all three mixtures used

in the different mixtures can be seen in table 3.5. Note that fines are defined as solids with a particle size of less than 17 μm.

Table 3.5: Fines fraction of different particle mixtures

Particle mixture	Percentage fines
Atomised FeSi	8.57%
Milled FeSi	1.78%
FeSi mixture	5.51%

Attrition

One of the negative influences of entrainment is that the particles tend to break up into smaller particles inside the cyclone as a result of the high collision rate and high linear velocities inside the cyclone as well as a lot of friction between the particles and the cyclone (Yang, 2003: p.207). This attrition may create a large amount of fines which cannot be removed by the cyclone and are lost inside the filters. To ensure that significant attrition does not occur inside the experimental setup, a comparison has to be done between fresh unused solids and spent solids after a long period of operation (More than a week of experimental time, or 24 hours time on stream). This can be seen in figure 3.4. The

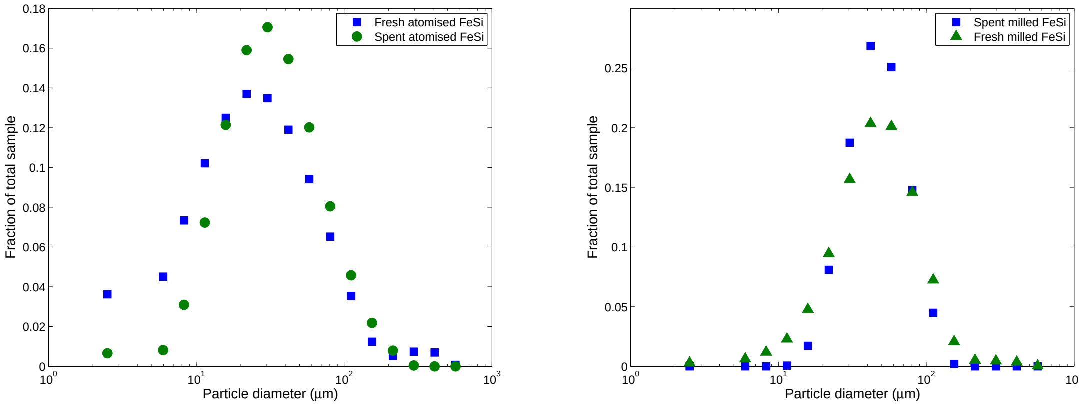

(a) The effect of attrition due to extensive entrainment on atomised FeSi

(b) The effect of attrition due to extensive entrainment on milled FeSi

Figure 3.4: Indication of how the PSD's of the FeSi mixtures change after an extended period inside the fluidised bed

PSD's inside the fluidised bed rapidly moved towards that of the spent FeSi profiles seen in the figure. It was therefore assumed that the PSD's in the fluidised bed at all times were that of the spent FeSi profiles. The combination mixture is made up of atomised and milled FeSi and for that reason the attrition effect was not tested on the combination mixture, as no significant attrition was found in either the atomised or the milled FeSi. Note that the mass of the filters were measured from time to time to know how much fines were lost in the cyclone. Care was taken therefore that the amount of fines captured in the filters were insignificant and that the entrainment measurements were not influenced.

Bed height

As noted in section 2.3.1, the height of the packed bed can influence the entrainment rate. The term 'deep bed' is often used when speaking of Geldart A powders, where the depth of the fluidised bed is sufficient so that a stable bubble size have been reached and a further increase in bed height will not influence the bubble properties. To ensure that a 'deep bed' is being used a batch of experiments were done with three different packed bed heights, namely 0.4 m, 0.6 m and 0.8 m. Bed heights of double the normal packing height, one and a half times the normal packing height and the normal packing height (0.4 m) were compared with each other. The results of these comparisons can be seen in table 3.6. The absolute average relative difference was used to compare the entrainment rates of the different bed heights and was calculated as:

$$\text{AARD} = \sum_{i}^{n} \frac{|\text{Entrainment rate}_{0.4\,\text{m}} - \text{Entrainment rate}_{\text{Compared height}}|}{\text{Entrainment rate}_{0.4\,\text{m}}} \frac{1}{n} \times 100$$

These relative differences associated with the difference in bed heights are rather small when compared with the repeatability results seen in table 3.4. Therefore it can be said with confidence that the bed depth of 0.4 m is sufficient to consider the fluidised bed as a deep bed.

Table 3.6: Relative difference in entrainment for different fixed bed heights with respect to the average value of entrainment at the normal fixed bed height

Solids mixture	Error compared to average values			
	1.5 × normal height		2 × normal height	
	AARD	Maximum	AARD	Maximum
Atomised FeSi	23.47%	40.19%	8.62%	18.02%
Milled FeSi	14.94%	24.18%	20.79%	26.55%
FeSi Mixture	7.76%	15.6%	4.92%	7.58%

3.3 Image Processing

Most shape characterisation techniques relies on the availability of an image of the particles so that the features used in shape characterisation can be measured. It is therefore necessary to have an image with a high enough resolution of the particle in question to be able to measure these features. The choice had to be made between using either a scanning electron microscope (SEM), or a normal light microscope with an attached camera. The light microscope is cheaper and easier to use but the depth of field that it can focus on at any time is very shallow. This results in the problem that only a section of the particle under investigation will be visible. The SEM is much more cumbersome to use and expensive, but it has a much deeper depth of field in focus. A comparison of the images that the two microscopes can take can be seen in figure 3.5. The light microscope is able to show detail inside the perimeter of the particle but the area of interest for image processing is the perimeter of the particle. The perimeter of the particles in the light microscope images are rather smudged. The perimeters of the particles in the SEM images are properly in focus. With the detail in these images, a true representation of the particle perimeter can be obtained. The three dimensional nature of the particles

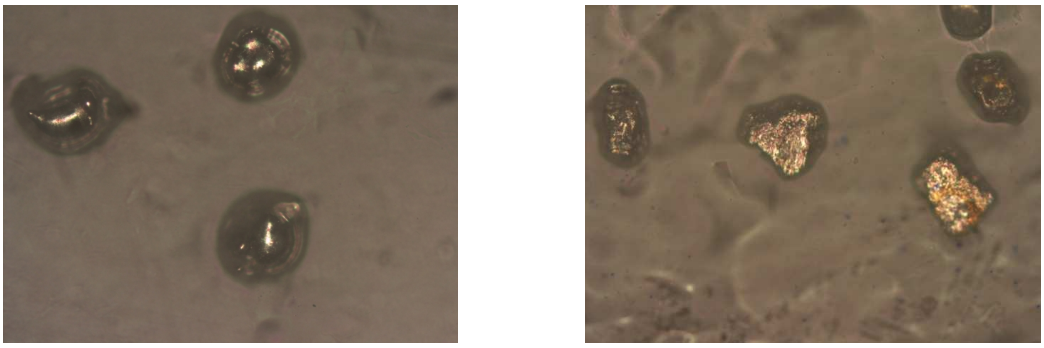

(a) Image of atomised FeSi particles as taken with light microscope

(b) Image of milled FeSi particles as taken with light microscope

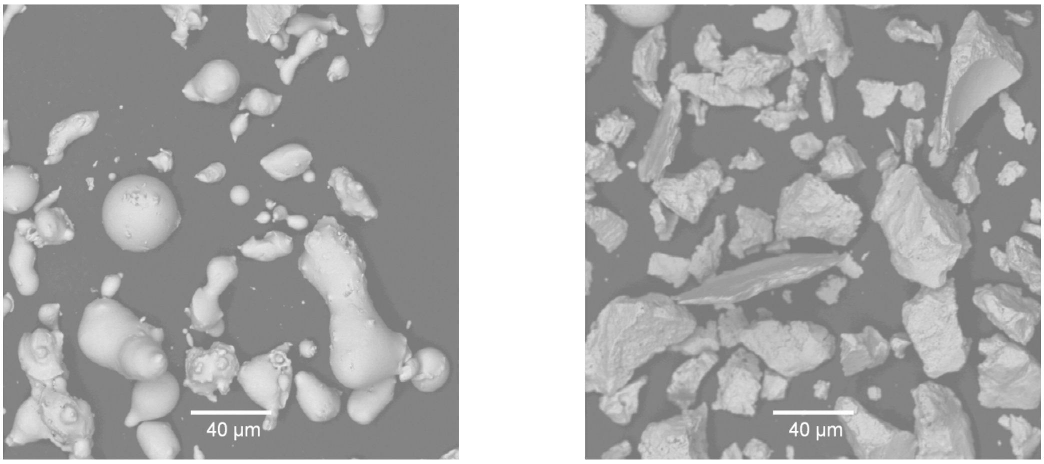

(c) Image of atomised FeSi particles as taken with SEM

(d) Image of milled FeSi particles as taken with SEM

Figure 3.5: Comparison between the quality of the images taken with the two types of microscopes

can also be seen in the SEM images, although it cannot be quantified with normal image processing techniques. With this extra ability, an additional, qualitative observation can be made of the differences between the two mixtures. The atomised particles tend to be mostly round, in other words all three dimensions are of a similar size. The milled particles appear to be mostly flakes, which means that two of the three dimensions are much larger than the third. This observation can not be made with a light microscope. These images therefore show how the light microscope is insufficient for the type of images required for shape description by image processing. The SEM used to capture all the images was a JEOL JSM-6300 Scanning Microscope.

To be able to do particle shape analysis with the images obtained from the SEM, these images had to be processed and manipulated in such a way that the particles are all available in Matlab as datasets which can then be processed further. The whole process of obtaining the particle data from the images as well as the consequent processing to analyse the particle shapes are explained in detail in appendix B.

CHAPTER 4

Results and discussion

4.1 Fluidisation characteristics

4.1.1 Minimum fluidisation

The minimum fluidisation velocity of a fixed bed can give a good indication of the internal structure of the bed. The minimum fluidisation velocity was measured by measuring the pressure drop over the fixed bed up to the point of fluidisation. The results of these measurements can be seen in figure 4.1. These results show that a much larger drag on the milled FeSi particles are required to overcome the gravitational and cohesive forces between the particles and fluidise the bed. Since the densities of both the atomised and the milled FeSi are the same, the reason for this higher energy requirement for fluidisation

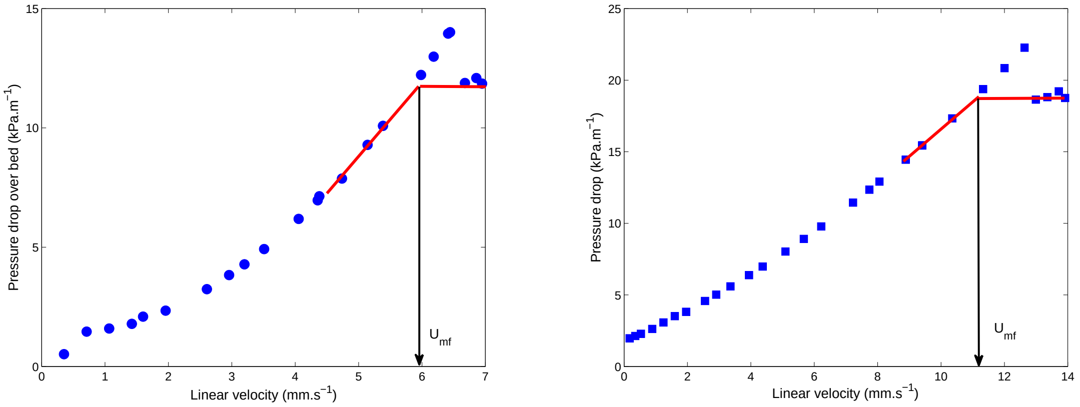

(a) Pressure drop profile over the fixed bed for the atomised FeSi ($U_{mf} = 6\,{}^{mm}/_{s}$)

(b) Pressure drop profile over the fixed bed for the milled FeSi ($U_{mf} = 11\,{}^{mm}/_{s}$)

Figure 4.1: Results of the minimum fluidisation velocity measurements for both the atomised and milled FeSi

has to be either the terminal velocity of the milled FeSi or the cohesive forces between the milled FeSi particles, or a combination of these two effects. Note that the slightly higher pressure drop for the atomised FeSi can be attributed to a lower voidage in the bed, because as can be seen in table 3.1, the packing density of the milled FeSi is lower than that of the atomised FeSi. The increased pressure drop can also be caused by more frictional drag on the atomised FeSi compared to the milled FeSi, or the more likely explanation, the more tortuous pores inside the atomised FeSi fixed bed result in longer paths for the gas to flow through, which causes the higher pressure drop.

4.1.2 Solids entrainment

The results of the comparison between the entrainment rates for all the particle mixtures can be seen in figure 4.2. It is quite obvious that the atomised FeSi has a significantly higher entrainment rate than the milled FeSi. To quantify this difference, on average the entrainment rate for the atomised FeSi is about six times higher than that of the milled FeSi.

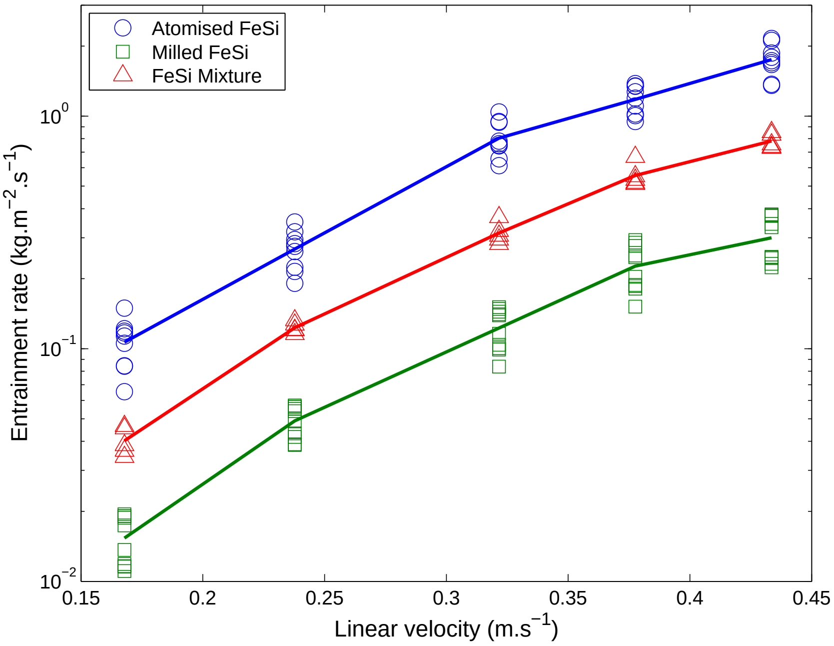

Figure 4.2: Comparison of the entrainment rates for the different solid mixtures. Solid lines represent the average values for the individual mixtures

The effect of the different fines concentrations

It is important to remember that this big difference in entrainment rates might be as a result of the higher fines concentration in the atomised FeSi, as seen in table 3.5. In attempt to disprove that the difference in fines concentration is only reason why the entrainment rates of the mixtures differed, a third mixture of FeSi was made up. This mixture contained 50% atomised and 50% milled FeSi by mass. If the increased entrainment rate was caused only by the difference in particle size distribution, the mixture should have an entrainment rate which is exactly halfway between the atomised and the milled FeSi. Therefore, if a graph is constructed where the entrainment rate is plotted as a function of the fraction atomised FeSi in the mixture, a straight line should be seen between the milled FeSi (fraction atomised FeSi = 0) and the atomised FeSi (fraction atomised FeSi = 1). To illustrate this better, theoretical mixtures of FeSi were made up from the atomised and milled FeSi PSD's ranging from an atomised FeSi fraction of 0.1 to an atomised FeSi fraction of 0.9. Together with the actual PSD's of the milled and the atomised FeSi, these theoretical mixtures were used to predict the elutriation rate constant with the correlation developed by Geldart et al. (1979). The results of these predictions can be seen in figure 4.3. A sphericity of 1 was used to calculate the terminal velocities of the solids, therefore the results are not influenced by shape, but will only predict the resultant effect of mixing two different mixtures with two different PSD's on entrainment rate. Assuming that the correlation of Geldart et al. (1979) is accurate, the straight line relationship seen in figure 4.3 proves that if two mixtures of equal densities but with different PSD's are mixed, the entrainment rate is linearly dependent on the fractions of the two mixtures. Therefore, if the higher entrainment rate of the atomised FeSi compared to the milled FeSi as seen in figure 4.2 are caused by the difference in particle size only, a straight line relationship should be seen between the entrainment rates of the three different experimental mixtures and the fraction of atomised FeSi present in the mixtures. The measured relationship can be seen in figure 4.4. The results shown

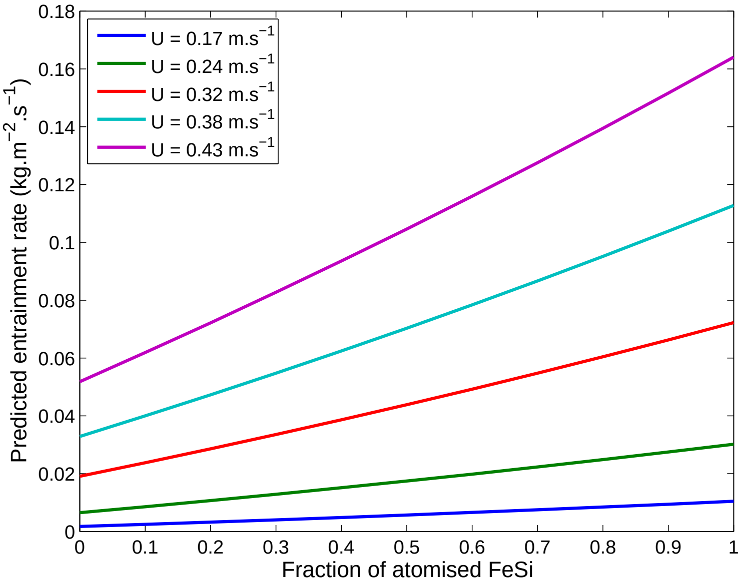

Figure 4.3: Prediction of how the entrainment rate should vary as the fraction of atomised FeSi in a FeSi mixture changes according to Geldart et al. (1979).

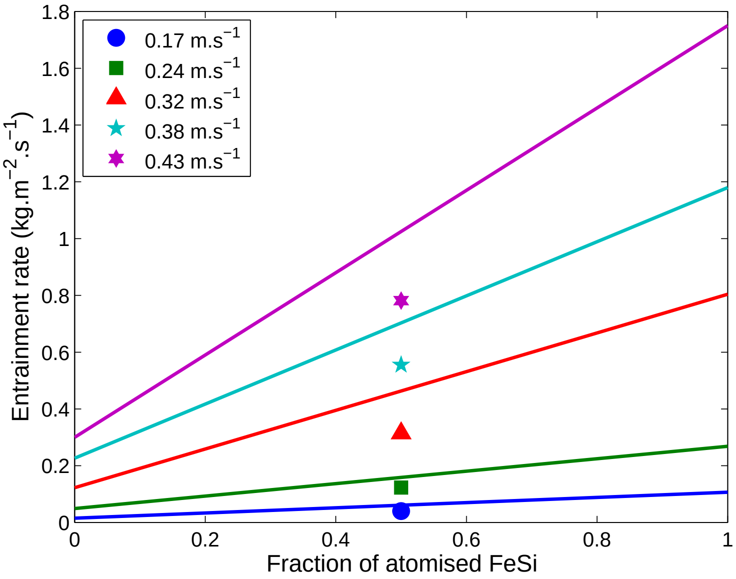

Figure 4.4: Experimental results of how entrainment rates vary as a function of the fraction of atomised FeSi in the solid mixture. Straight lines represent the theoretical relationships where the PSD is the only factor that influences the entrainment rates.

are a good indication that the difference in the PSD's for the atomised and the milled FeSi are not solely responsible for the difference in entrainment rates, but that another factor, namely particle shape, has to play a role.

4.2 Shape analysis results

From the SEM photos seen in section 3.3 there appears to be a very big difference in particle shapes of the different mixtures. It is therefore necessary to see if it is possible to quantify the difference in shape between the different solids. Most of the techniques described in appendix A were used to quantify the difference in shape between the atomised and the milled FeSi mixtures. The performance of the techniques can be seen in table 4.1. Note that the absolute relative difference was calculated as:

$$\text{ARD} = \frac{|\text{Value of shape descriptor}_{\text{Atomised}} - \text{Value of shape descriptor}_{\text{Milled}}|}{\text{Value of shape descriptor}_{\text{Atomised}}} \times 100 \quad (4.1)$$

Of all the shape description techniques tested, only the circularity had the ability to distinguish properly between shapes of the different particle mixtures. Therefore only the circularity will be discussed in this section.

Table 4.1: Comparison between the performance of the different shape description techniques

Shape descriptor	Absolute relative difference
Circularity	9.08%
Fractal dimension	0.79%
Piper's angle	0.33%
Persistence of 2nd harmonic	2.53%
Persistence of 3rd harmonic	3.96%
Persistence of 4th harmonic	0.10%
Persistence of 5th harmonic	0.39%

4.2.1 Circularity

Although sphericity for such small particles is difficult to measure with normal techniques (Thompson & Clark, 1991), the circularity is a very easy parameter to measure if two dimensional images of a particle is available. Circularity can be calculated by using the surface areas of the particle projections as well as their perimeter length. The perimeter of a circle with the same surface area as that of the particle under investigation can then be calculated and compared to the known perimeter. A comparison of the circularity for both mixtures can be seen in figure 4.5. It can be seen that both mixtures have a relatively wide distribution in circularities, with the distribution of the atomised FeSi shifted closer to a circularity of 1. Both mixtures have a large fraction of relatively circular particles though, which can disqualify circularity as a good shape descriptor since it does not distinguish between the different mixtures well enough. Note that most of the milled FeSi particles are lying in their most stable position, which can make them appear more spherical than they are.

4.2.2 Other techniques

The big overlap in circularities for the atomised and the milled FeSi indicated the need for another shape characterisation technique that can distinguish better between the different particle shapes. However, the performance of all the other techniques in appendix A were shown in table 4.1 where it was indicated that circularity performed the best in the

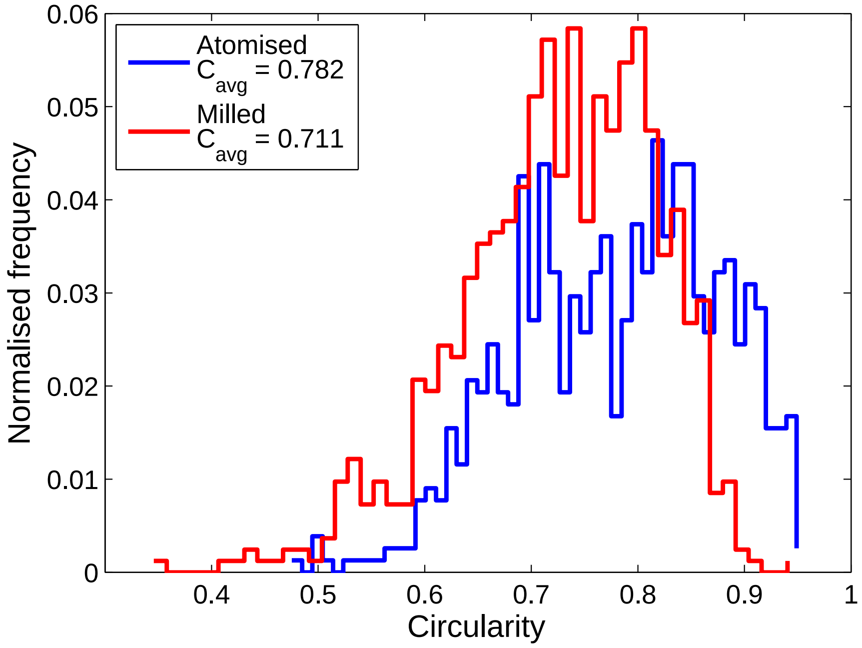

Figure 4.5: The circularity of both the atomised and the milled FeSi as a frequency plot. C_{avg} for the atomised FeSi = 0.782 and C_{avg} for the milled FeSi = 0.711

techniques tested. A more complete display of these results as well as a discussion of the results for these other shape descriptors can be seen in appendix C. The problem with most of the techniques in literature is that they characterise a particle shape based on a two dimensional image. This can be accurate, but it can also mislead one into believing that a particle is a sphere, when it is actually a thin disk. However, due to the lack of anything better, the particle circularity will be used as the shape descriptor of choice in this study. As is done in literature (Smolders & Bayens, 1997), the circularity will be used in the same way as a sphericity. This means that in the drag coefficient correlation (Equation 2.10), the sphericity will simply be replaced with the circularity. This has to be done, as no other proper shape descriptor is available.

4.3 Understanding particle shape effects in entrainment

The entrainment rate is definitely influenced by the shape of the particles that is fluidised, as was shown in this chapter. How this occurs can possibly be explained by one or more of the following ideas:

- The way the particle orientates itself as the gas flows over it can significantly affect the terminal velocity of the particle

- The orientation of particles can influence the direction into which particles shoot off after a collision between two particles.

- The Van der Waals forces between the particles are affected by the particle shape

Isaacs & Thodos (1967) reported that cylinders orientate themselves differently when settling in water, depending on the ratio between the diameter and the length of the cylinder. This behaviour have been attributed to the formation of vortexes around and behind the cylinders which then induces secondary forces on the cylinders. This type of behaviour is also possible in the fluidised bed. Particles like the milled FeSi, which are flaky in nature, can orientate themselves in such a way that the coefficient of drag is minimised and that they require a larger gas flow rate to keep them entrained. However, this is hard to proof directly, as the particles are extremely small, and would therefore require a special setup that includes a microscope to see how they orientate themselves at different flow rates. However, the behaviour of a lot of particles together in a fluid and a single particle in a fluid can hardly be assumed to be similar. The large amount of collisions found inside the freeboard of a fluidised bed will in all likelihood cancel out any effects that particle shape will have on the orientation of a particle in the freeboard.

When a sphere drifts in the fluidising air and another sphere collides with the sphere, the direction into which the sphere shoots off is not influenced by the orientation of the sphere. This happens because the centre of mass of a sphere is the same distance from every point on the surface of that sphere. However, when a non spherical particle is collided with, the direction into which the particle shoots off is a function of the orientation of the particle. This means that when another particle collides with the corner of a flake-like particle, the particle might veer off into a different direction since the particle impact caused the particle to rotate around its centre of mass. What all of this boils down to is that more spherical particles have a larger probability to have elastic collisions while non-spherical particles tend to have less elastic collisions. However, this is a lot of speculation and needs to be investigated further before any further statements can be made.

Baeyens et al. (1992) as well as Ma & Kato (1998) noted that the Van der Waals forces between a sphere and a plane is larger than the Van der Waals forces between two spheres. This is as a result of the centres of mass of the two objects being able to move much closer together. The shape of the milled FeSi, which is flaky, can therefore allow for much larger Van der Waals forces between the particles. This will in turn result in a larger number of clusters forming that will reduce the entrainment rate, as clusters tend to fall back to the bed, while single particles are entrained and removed from the freeboard. If shape affects the inter-particle forces, one would expect the more spherical particles to entrain quicker and at lower velocities with the less spherical particles only getting entrained at higher velocities where the momentum of the particles is sufficiently large enough to overcome the Van der Waals forces. Proof of this theory is given in figure 4.6. This

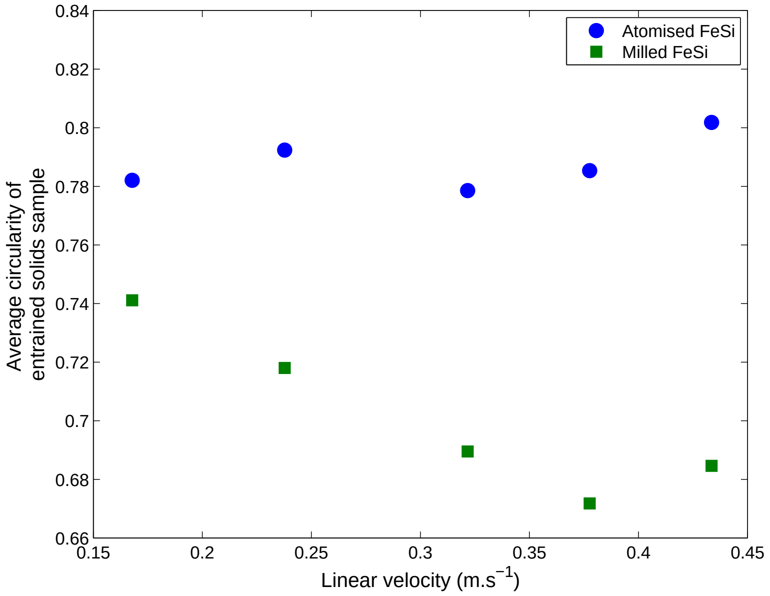

Figure 4.6: Illustration of how the average circularity of entrained solids change as the linear velocity at which they were entrained increases

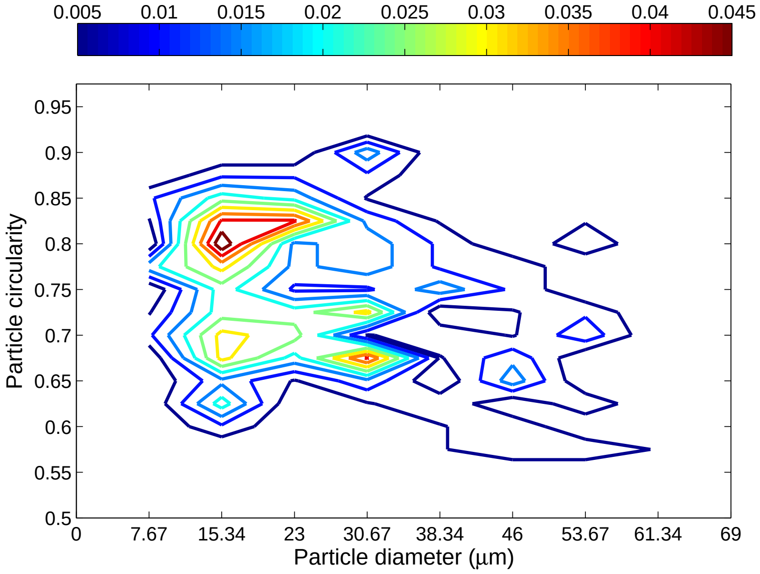

Figure 4.7: An indication of how the particle circularity is distributed as a function of particle diameter (Data from sample of atomised FeSi particles). Contours represent normalised frequencies. Note the high circularity of the small particles.

figure shows how the average circularity of the entrained particles changes as the velocity with which the particles are removed from the bed increases. For the atomised FeSi, no clear trend can be seen, as the difference in circularity is within experimental error. This can be explained by the large amount of highly circular atomised FeSi particles of the size fraction that gets entrained, as seen in figure 4.7. However, the milled FeSi shows a clear trend. At low velocities the particles with high circularities, i.e. those that do not form clusters as easily, are entrained and removed from the freeboard. As the gas velocity increases, the momentum of the individual particles in the cluster are sufficiently large enough to escape the clusters. The speed at which clusters collide with each other and the reactor walls are also large enough to cause break-up of the clusters or ejection of some of the particles in the clusters.

4.4 Predicting entrainment rates

In order to see which of the popular elutriation rate constants performs the best in predicting the behaviour of the FeSi mixtures, all of the correlations were compared to the experimental results. The ability of these models to include the effect of particle shape should also be evaluated. As circularity is the shape descriptor with the best performance in differentiating between the particle shapes of the different mixtures, it will be used instead of a sphericity to adjust for the particle terminal velocity where applicable. The performance of these correlations can be seen in table 4.2. Note that the AARE is defined in this case as:

$$\text{AARE} = \sum_{i}^{n} \frac{|\text{Entrainment rate}_{\text{Measured}} - \text{Entrainment rate}_{\text{Predicted}}|}{\text{Entrainment rate}_{\text{Measured}}} \frac{1}{n} \times 100 \tag{4.2}$$

The poor performance of all the different correlations in predicting the entrainment rates for the mixtures once again shows the extreme importance in doing actual experiments to see which model fits the data the best. In this case the model of Choi et al. (1999) worked the best over the range of mixtures, with the model of Geldart et al. (1979) having a similar accuracy in predicting the entrainment rates. However, the model of Geldart et al. (1979) is preferable to that of Choi et al. (1999) as the shape of the model approximates the shape of the experimental data better as can be seen in figure 4.8. In this case, with a shape descriptor in the model i.e. the circularity, the model performs better, as seen in the figure. However, this will not always be true. If a model is found that has a relatively good error in predicting the experimental data, but the model systematically predicts higher entrainment rates than the experimental data, the model will perform worse when using a sphericity when correcting for shape.

Table 4.2: Performance of different elutriation rate correlations in predicting the experimental entrainment rates for the different solid mixtures

Model	AARE between the prediction of the models and the measured entrainment rate of the various particle mixtures		
	Atomised FeSi	Milled FeSi	FeSi mixture
Yagi & Aochi (1955)	249%	1823%	553%
Zenz & Weil (1958)	601%	2217%	1262%
Wen & Hashinger (1960)	100%	100%	100%
Tanaka et al. (1972)	94.2%	90.1%	88.7%
Merrick & Highley (1974)	552%	1375%	1154%
Geldart et al. (1979)	87.5%	75.2%	74.4%
Lin et al. (1980)	495%	2051%	1084%
Colakyan & Levenspiel (1984)	99.4%	96.2%	98.8%
Subbarao (1986)	100%	100%	100%
Ściążko et al. (1991)	87.8%	78.1%	75.6
Baeyens et al. (1992)	163%	1431%	412%
Nakagawa et al. (1994)	57.7%	390%	96.7%
Tasirin & Geldart (1998)	95.6%	97.1%	97.1%
Choi et al. (1999)	84.1%	71.7%	62.1%

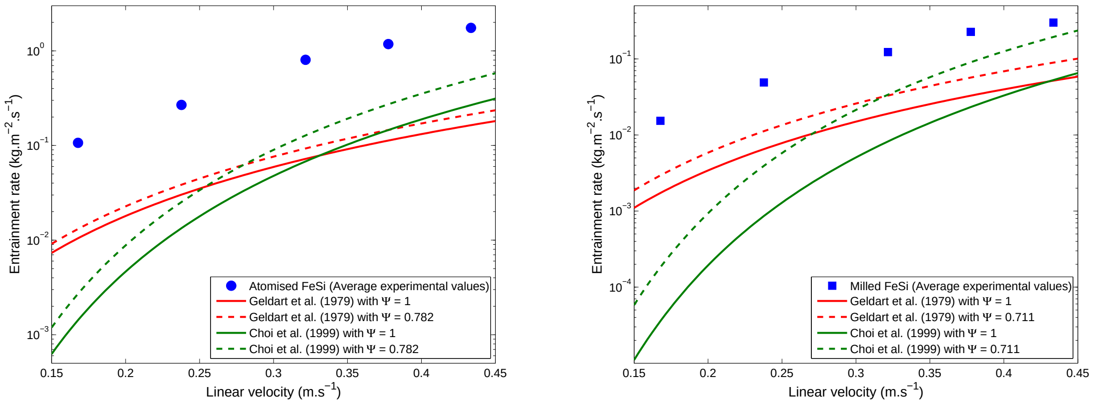

(a) Entrainment rate for atomised FeSi

(b) Entrainment rate for milled FeSi

Figure 4.8: Entrainment rate as measured on the experimental setup together with the predictions of the correlations by Geldart et al. (1979) and Choi et al. (1999)

It is possible to do an adjustment to the elutriation rate constant correlation of Geldart et al. (1979) where the shape is taken into account more seriously, but the only shape factor available at this point is the circularity. Circularity is flawed in that it does not take three dimensional shape effects into account, which means that disks and spheres would have the same circularity. It seems therefore rather pointless to adjust an existing correlation with a less than perfect shape descriptor – this will be left for a further study.

CHAPTER 5

Conclusions and Recommendations

5.1 Conclusions

Particle shape effects on entrainment in gas–solid fluidisation and have been studied in a 140 mm perspex column using two different FeSi mixtures namely atomised FeSi and milled FeSi. The atomised FeSi had a fines concentration of 8.6% while the milled FeSi had a fines concentration of 1.8%, but the solid densities of both mixtures were identical. The average particle diameter of the mixtures were 38 μm for the atomised FeSi and 50 μm for the milled FeSi. The following conclusions were drawn in this work:

- It was found that the atomised FeSi had a minimum fluidisation velocity of 6 $^{\mathrm{mm}}/_{\mathrm{s}}$ while the milled FeSi needed a gas velocity of 11 $^{\mathrm{mm}}/_{\mathrm{s}}$ to fluidise. This indicates that the milled FeSi has higher cohesion forces between the particles and/or has higher terminal velocities.

- The entrainment rate for the atomised FeSi was found to be in the order of six times higher than the entrainment rate of the milled FeSi over the entire range of the superficial velocities investigated.

- Although the higher concentration of fines in the atomised FeSi had an effect on the entrainment rate, it was proved that this was not nearly enough to explain the difference in the entrainment rates between the two particle types. It could therefore be concluded that the particle shape plays a significant role in entrainment of solids in a fluidised bed.

- Various different shape descriptor techniques were used in attempt to distinguish between the shapes of the different particle mixtures. All of the techniques used relies on a two dimensional projection of the particle, which is then further analysed.

All of these techniques, except for the circularity, failed to distinguish sufficiently between the different particle shapes. The average circularity for atomised FeSi was 0.782 compared to 0.711 for milled FeSi.

- The circularity was used instead of a sphericity to calculate the terminal velocity for the particle mixtures. The calculated terminal velocity was then used in the correlations to adjust for the effect of particle shape. All of the popular correlations had a poor prediction of the entrainment rates, with the correlations of Choi et al. (1999) and Geldart et al. (1979) having the best performance. These correlations had an AARE of 72.6% and 79% respectively for all of the mixtures used. These results show that the single particle drag is not sufficient to quantify the effect of particle shape on entrainment rate in fluidised beds.
- It is suggested that particle shape can cause a big difference in entrainment rates by affecting the cohesive behaviour of the particles in the freeboard. More spherical particles have a lower probability to form clusters than flake-like particles. This occurs because, regardless of the particle orientation, the distance between the centres of mass for two spherical particles are always relatively high, compared to non-spherical particles which can orientate in such a way that the centres of mass are relatively close to each other.
- Particle shape can also influence entrainment rate as a result of particle orientation. Regardless of the orientation of particles with a high sphericity, the projected area are always more or less the same, while the projected area of irregular particles are significantly affected by the particle orientation. The projected area of particles and consequently the terminal velocity of particles are influenced by particle orientation. However, the terminal velocity is an unlikely reason for the difference in entrainment rates. The way particles are deflected after collisions between each other can also be influenced substantially by the orientation and this is a more likely explanation of how particle orientation as a result of particle shape can influence entrainment rates.

5.2 Recommendations

A few areas for further investigation was identified in this study:

- It is necessary to develop a method and/or model to predict ‘bulk drag coefficients’ and ‘bulk terminal velocities’ so that these properties instead of single particle properties can be used in elutriation rate constant correlations.

- A three dimensional shape descriptor should be developed with emphasis on its ability to adjust for shape effects on hydrodynamic behaviour. This method should also be applicable to small particles where it is very difficult to obtain images at various particle orientations for the same particles.
- The mechanism through which particle shape influences entrainment rate should be studied. The contribution of particle shape to cohesive behaviour and cluster formation can be done by studying the effect of particle shape on entrainment at higher superficial velocities in the turbulent and the fast fluidisation regimes, as this study was limited to the bubbling regime. The contribution of particle shape on orientation and the consequent effect on entrainment should be studied by fluidising similar sized particle combinations (as with the atomised and milled FeSi) but with different shapes over a wide range of particle size distributions, as the effect of particle shape on cohesive behaviour will become less significant as the particle size increases.

BIBLIOGRAPHY

Adánez, J. and Abanades, J. (1991) "Minimum fluidization velocities of fluidized-bed coal-combustion solids", *Powder Technology, 67*, 113 – 119.

Aschenbrenner, B. C. (1956) "A new method of expressing particle sphericity", *Journal of Sedimentary Petrology, 26* (1), 15 – 31.

Baeyens, J.; Geldart, J. and Wu, Y. (1992) "Elutriation of fines from gas fluidized beds of Geldart A-type powders - Effect of adding superfines", *Powder Technology, 71*, 71 – 80.

Baron, T.; Briens, C. L.; Galtier, P. and Bergougnou, M. A. (1990) "Effect of bed height on particle entrainment from gas fluidized beds", *Powder Technology, 63*, 149 – 156.

Cai, P.; Schiavetti, M.; De Michele, G.; Grazzini, G. C. and Miccio, M. (1994) "Quantitative estimation of bubble size in PFBC", *Powder Technology, 80*, 99 – 109.

Chan, H. and Knowlton, T. M. (1984) "The effect of system pressure on the transport disengagement height (TDH) above bubbling gas-fluidized beds", *AIChE Symposium Series, 80* (241), 24 – 33.

Chaplin, G.; Pugsley, T. and Winters, C. (2005) "The S-statistic as an early warning of entrainment in a fluidized bed dryer containing pharmaceutical granule", *Powder Technology, 149*, 148 – 156.

Chitester, D. C.; Kornosky, R. M.; Fan, L. S. and Danko, J. P. (1984) "Characteristics of fluidization at high pressure", *Chemical Engineering Science, 39* (2), 253 – 261.

Choi, J. H.; Chang, I. Y.; Shun, D. W.; Yi, C. K.; Son, J. E. and Kim, S. D. (1999) "Correlation on the particle entrainment rate in gas fluidized beds", *Ind. Eng. Chem. Res., 38*, 2491 – 2496.

Choi, J. H.; Son, J. E. and Kim, S. D. (1989) "Solid entrainment in fluidized bed combustors", *Journal of Chemical Engineering of Japan, 22* (6), 597 – 606.

Choi, J. H.; Song, J. E. and Kim, S. D. (1998) "Generalized model for bubble size and frequency in gas-fluidized beds", *Ind. Eng. Chem. Res., 37*, 2559 – 2564.

Clark, N. N. (1987) "A new scheme for particle shape characterization based on fractal harmonics and fractal dimensions", *Powder Technology, 51*, 243 – 249.

Clark, N. N.; Gabriele, P.; Shuker, S. and Turton, R. (1989) "Drag coefficient or irregular particles in Newton's settling regime", *Powder Technology, 59*, 69 – 72.

Colakyan, M. and Levenspiel, O. (1984) "Elutriation from fluidized beds", *Powder Technology, 38*, 223 – 232.

Cutbill, J. L. (Ed.) (1971) *Data processing in Biology and Geology*, Academic Press, London.

Drolon, H.; Druaux, F. and Faure, A. (2000) "Particles shape analysis and classification using the wavelet transform", *Pattern Recognition Letters, 21*, 473 – 482.

Drolon, H.; Hoyes, B.; Druaux, F. and Faure, A. (2003) "Multiscale roughness analysis of particles: Application to the classification of detrital sediments", *Mathematical Geology, 35* (7), 805 – 817.

Du, B.; Warsito, W. and Fan, L. S. (2005) "ECT studies of gas-solid fluidized beds of different diameters", *Ind. Eng. Chem. Res., 44*, 5020 – 5030.

Ergun, S. (1952) "Fluid flow through packed columns", *Chemical Engineering Progress, 48* (2), 89 – 94.

Flemmer, R. L. C.; Pickett, J. and Clark, N. N. (1993) "An experimental study on the effect of particle shape on fluidization behaviour", *Powder Technology, 77*, 123 – 133.

Fong, S. T.; Beddow, J. K. and Vetter, A. F. (1979) "A refined method of particle shape representation", *Powder Technology, 22*, 17 – 21.

Geldart, D. (1973) "Types of gas fluidization", *Powder Technology, 7*, 285 – 292.

Geldart, D.; Cullinan, J.; Georghiades, S.; Gilvray, D. and Pope, D. J. (1979) "The effect of fines on entrainment from gas fluidized beds", *Trans IChemE, 57*, 269 – 275.

Geldart, D. and Pope, D. (1983) "Interaction of fine and coarse particles in the freeboard of a fluidised bed", *Powder Technology, 34*, 96 – 97.

George, S. E. and Grace, J. R. (1978) "Entrainment of particles from an aggregative fluidized bed", *AIChE Symposium Series, 74*, 67 – 74.

George, S. E. and Grace, J. R. (1981) "Entrainment of particles from a pilot scale fluidized bed", *The Canadian Journal of Chemical Engineering, 59*, 279 – 284.

Haider, A. and Levenspiel, O. (1989) "Drag coefficient and terminal velocity of spherical and non-spherical particles", *Powder Technology, 58*, 63 – 70.

Harrison, D.; Davidson, J. F. and Kock, J. W. D. (1961) "On the nature of aggregative and particulate fluidization", *Trans. Inst. Chem. Eng., 39*, 202 – 211.

Heywood, H. (1962) "Uniform and non-uniform motion of particles in fluids", *Interaction between fluids & particles,* pages 1 – 8.

Isaacs, J. L. and Thodos, G. (1967) "The free-settling of solid cylindrical particles in the turbulent regime", *Canadian Journal of Chemical Engineering, 45*, 150.

Kato, K.; Tajima, T.; Mao, M. and Iwamoto, H. (1985) *Fluidization – '85*, Elsevier, Science and Technology Amsterdam.

Kunii, D. and Levenspiel, O. (1991) *Fluidization Engineering*, Butterworth – Heinemann, Boston.

Levy, E. K.; Caram, H. S.; Dille, J. C. and Edelstein, S. (1983) "Mechanisms for solid ejection from gas-fluidized beds", *AIChE Journal, 29* (3), 383 – 388.

Lin, L.; Sears, J. T. and Wen, C. Y. (1980) "Elutriation and attrition of char from a large fluidized bed", *Powder Technology, 27*, 105 – 115.

Ma, A. and Kato, K. (1998) "Effect of interparticle adhesion forces on elutriation of fine powders from a fluidized bed of a binary particle mixture", *Powder Technology, 95*, 93 – 101.

Mandelbrot, B. B. (1977) *Fractals: Form, Change and dimension*, Freeman, San Francisco.

Merrick, D. and Highley, J. (1974) "Particle size reduction and elutriation in a fluidized bed process", *AIChE Symposium Series, 70* (137), 366 – 378.

Nakagawa, N.; Arita, S.; Uchida, H.; Takamura, N.; Takarda, T. and Kato, K. (1994) "Particle hold-up and elutriation rate in the freeboard of fluid beds", *Journal of Chemical Engineering of Japan, 27* (1), 79 – 84.

Newland, D. E. (1993) "Harmonic wavelet analysis", *Proceedings of the Royal Society of London: A: Mathematical and Physical Sciences, 443* (1917), 203 – 205.

Pemberton, S. T. and Davidson, J. F. (1984) "Turbulence in the freeboard of a gas fluidized bed", *Chemical Engineering Science, 39*, 829 – 840.

Pemberton, S. T. and Davidson, J. F. (1986) "Elutriation from fluidized beds – I. Particle ejection from the dense phase into the freeboard", *Chemical Engineering Science, 41* (2), 243 – 251.

Peters, M. H.; Fan, L. S. and Sweeney, T. L. (1983) "Study of particle ejections in the freeboard region of a fluidized bed with an image carrying probe", *Chemical Engineering Science, 38* (3), 481 – 485.

Pickett, J.; Clark, N. and Shuker, S. (1991) "A re-examination of Piper's shape analysis technique", *Partical and Partical System Characterization, 8*, 110 – 115.

Rietema, K. (1984) "Powders, what are they ?", *Powder Technology, 37*, 5 – 23.

Rowe, P. N. (1976) "Prediction of bubble size in a gas fluidised bed", *Chemical Engineering Science, 31*, 285 – 288.

Santana, D.; Rodríguez, J. M. and Macías-Machín, A. (1999) "Modelling fluidized bed elutriation of fine particles", *Powder Technology, 106*, 110 – 118.

Ściążko, M.; Brandrowski, J. and Raczek, J. (1991) "On the entrainment of solid particles from a fluidized bed", *Powder Technology, 66*, 33 – 39.

Smit, P. W.; Baloyi, S. and Shingles, T. "Cyclone performace in turbulent fluidized bed synthol reactors", Fluidization XI (2004).

Smolders, K. and Bayens, J. (1997) "Elutriation of fines from gas fluidized beds: Mechanisms of elutriation and effect of freeboard geometry", *Powder Technology, 92*, 35 – 46.

Sookai, S.; Carsky, M. and Baloyi, S. "Results of fluidized-bed hydrodynamic and entrainment studies for powders varying in particle size, density and shape", pages 211 – 221 Industrial Fluidization South Africa (2005).

Subbarao, D. (1986) "Cluster and lean-phase behaviour", *Powder Technology, 46*, 101 – 107.

Tanaka, I.; Shinohara, H.; Hirose, H. and Tanaka, Y. (1972) "Elutriation of fines from fluidized beds", *Journal of Chemical Engineering of Japan, 5* (1), 57 – 62.

Tasirin, S. M. and Geldart, D. (1998) "Entrainment of FCC from fluidized beds – A new correlation for the elutriation rate constant $K^*_{i\infty}$", *Powder Technology, 95*, 240 – 247.

Thompson, T. L. and Clark, N. N. (1991) "A holistic approach to particle drag prediction", *Powder Technology, 67*, 57 – 66.

Wadell, H. (1933) "Sphericity and roundness of rock particles", *The Journal of Geology, 41*, 310 – 331.

Wadell, H. (1934) "The coefficient of resistance as a function of Reynolds number for solids of various shapes", *Journal of the Franklin Institute, 217*, 459 – 490.

Wen, C. Y. and Chen, L. H. (1982) "Fluidized bed freeboard phenomena: Entrainment and elutriation", *AIChE Journal, 28* (1), 117 – 128.

Wen, C. Y. and Hashinger, R. F. (1960) "Elutriation of solid particles from a dense-phase fluidized bed", *AIChE Journal, 6* (2), 220 – 226.

Yagi, S. and Aochi, T. "Paper presented", Society of Chemical Engineers (Japan) Spring (1955).

Yang, W. C. (Ed.) (2003) *Handbook of Fluidization and Fluid-Particle Systems*, Marcel Dekker Inc, New York.

Yang, W. C. (2007) "Modification and re-interpretation of Geldart's classification of powders", *Powder Technology, 171*, 69 – 74.

Yerushalmi, J. and Cankurt, N. T. (1979) "Further studies of the regimes of fluidization", *Powder Technology, 24*, 187 – 205.

Yórquez-Ramírez, M. I. and Duursma, G. R. (2000) "Study of the flow pattern above an erupting bubble in an incipiently fluidised bed using image shifting", *Chemical Engineering Science, 55*, 2055 – 2064.

Yórquez-Ramírez, M. I. and Duursma, G. R. (2001) "Insights into the instantaneous freeboard flow above a bubbling fluidised bed", *Powder Technology, 116*, 76 – 84.

Zahn, C. T. and Roskies, R. Z. (1972) "Fourier descriptors for plane closed curves", *IEEE Transactions On Computers, C-21*, 269 – 281.

Zenz, F. A. and Weil, N. A. (1958) "A theoretical-emperical approach to the mechanism of particle entrainment from fluidized beds", *AIChE Journal, 4* (4), 472 – 479.

APPENDIX A

Particle shape description

More often than not, the particles of interest are not spherical, but come in all kinds of shapes. Various methods exist to describe this deviation from regular shapes, but these methods normally rely on choosing two characteristic parameters from

- Volume of the particle
- Surface area of the particle
- Projected area of the particle
- Projected perimeter of the particle.

The problem with these correlations developed to describe the particle shape is that for two seemingly very different particles, the shape descriptor can have similar values. It is therefore important to understand how these descriptors are derived to be able to use the correct descriptor for a certain application (Yang, 2003: p.3).

A.1 Classic techniques

The classic techniques used in shape description of particles mostly rely on simple and easy to use methods. Where easy direct measurements are not possible, inferred measurements are used. These techniques also rely heavily on tables filled with constants determined for certain particles. These constants can then be used to estimate what the shape of an other, completely unrelated, particle is.

In addition to the sphericity and circularity discussed in section 2.3.3 there is one other additional classic shape description technique. This technique is the Heywood shape factor.

A.1.1 Heywood shape factor

Heywood (1962) developed a empirical parameter that uses the projected area of the particle as a shape descriptor:

$$k = \frac{V_p}{{d_a}^3} \tag{A.1}$$

with

$$d_a = \sqrt{\frac{4A_p}{\pi}} \tag{A.2}$$

This shape descriptor has the same limiting problem as seen with sphericity. It is difficult to calculate the surface area of the particle, especially with very small particles. However, Heywood (1962) had a solution for this problem. It was suggested to estimate the value of k from the corresponding k_e of similar isometric particles by using equation A.3.

$$k = \frac{k_e}{e_1\sqrt{e_2}} \tag{A.3}$$

A list of the values of k_e for some regular shapes can be found in Heywood (1962). Heywood believed that k can be employed to correlate the drag on the particle and the terminal velocity of the particle with the help of d_a and the projected area to calculate Re and C_d.

A.2 Modern techniques

The modern techniques for shape description of particles are almost invariably used in conjunction with image processing. The accuracy of these techniques are therefore very much a function of how good the image as well as the preprocessing of the image is.

A.2.1 Fourier descriptors

When the perimeter of the two dimensional image of a particle is rolled out, a relationship between the angle and radius of the particle can be found. An example of this can be seen in figure A.1. This relationship will only be a straight line for a perfectly spherical particle. In the case of a non-spherical particle, the relationship normally shows some periodic behaviour. This periodic behaviour can be modelled with the Fourier expansion by adjusting the value of the harmonic amplitudes, A_i. For most particles, the harmonic order, n, should be relatively high.

Any periodic function with a period of 2π can be described by a Fourier series as:

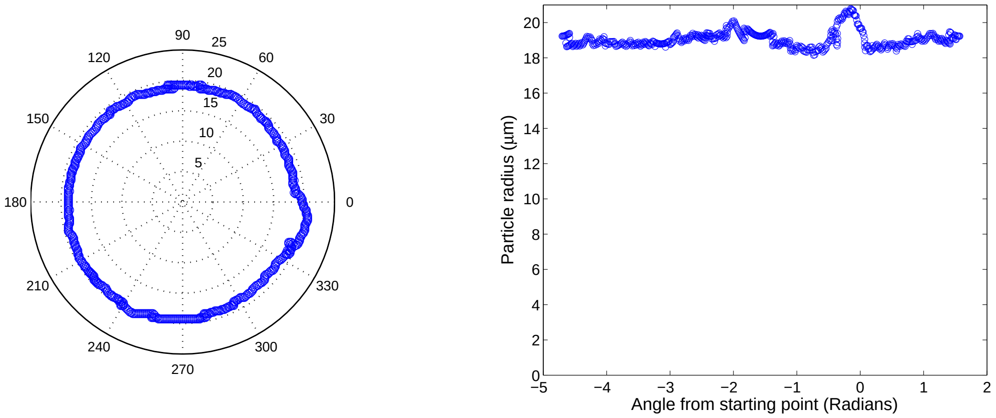

(a) Particle with high sphericity

(b) Rolled out perimeter of particle with high sphericity

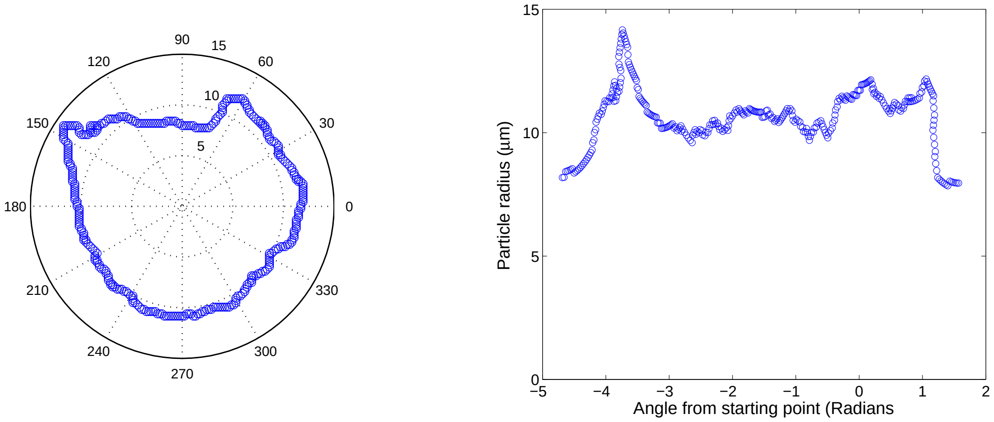

(c) Particle with lower sphericity

(d) Rolled out perimeter of particle with lower sphericity

Figure A.1: Example of how the particle shape can affect the periodicity of the rolled out particle perimeter

$$f(\theta) = a_0 + \sum_{n=1}^{N} \left[a_n \cos(n\theta) + b_n \sin(n\theta)\right] \tag{A.4}$$

This Fourier series is used more commonly in shape description as:

$$f(\theta) = A_0 + \sum_{n=1}^{N} \left[A_n \cos(n\theta + \phi_n)\right] \tag{A.5}$$

Fourier descriptors are good enough to describe particles that are close to spherical, but as soon as the particle show re-entrant behaviour, the ability of the Fourier descriptors to describe the particle shape breaks down (Clark, 1987). Re-entrant behaviour can be classified as the event where one angle value has more than one radius value associated with it. This problem can be circumvented by using the method developed by Zahn & Roskies (1972). This method have been reported to handle re-entrant shapes very well (Fong et al., 1979). The Zahn & Roskies method uses a specified length to walk around the particle. The change in angle as a function of the length walked is then plotted. The problem with Fourier descriptors is that as already stated, a fairly large amount of coefficients are required to describe complex particle shapes. The comparison of these coefficients can become very convoluted.

A.2.2 Fractal dimension

The idea of a fractal dimension was first used by Mandelbrot (1977) where the problem of the length of the coast of Britain was discussed. The problem exists where the size of the features taken into account affects the measured length of the coast. In other words, if the coast is measure in increments of 1 km, small bays and capes will not be ‘seen’, while if increments of 10 m is used, even large boulders will be ‘seen’. An example of this is illustrated in figure A.2. With smaller features taken into account the length of the coast will increase. This means that when atoms is taken into account, the length of the coast is effectively infinite. The relationship between the features taken into account, or step length (SL), and the measured length (ML) can be described as:

$$\mathrm{ML} \propto \mathrm{SL}^{S} \tag{A.6}$$

The fractal dimension have been defined as:

$$D_f = 1 - \mathrm{S} \tag{A.7}$$

The fractal dimension is a measure of the ability of a line to fill the space in which it exists. As the fractal dimension increase, the line has more kinks and micro structures. The fractal dimension for a 1-dimensional line in a 2-dimensional surface is limited to a

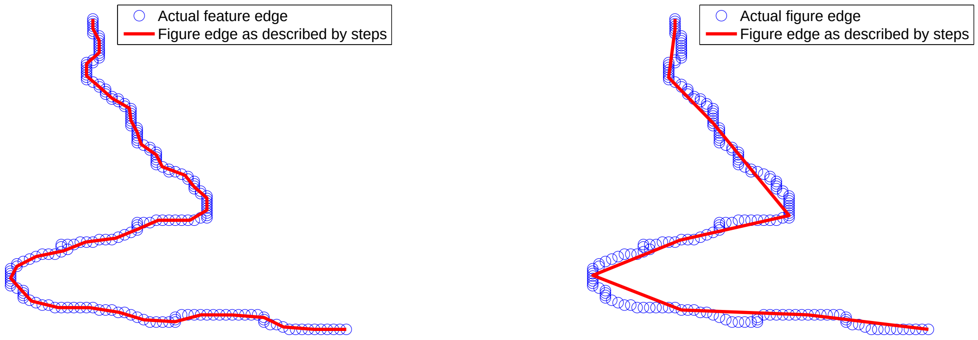

(a) Arbitrary figure edge measured with a small measurement length

(b) Arbitrary figure edge measured with a large measurement length

Figure A.2: Example of how the measurement length can affect the perimeter length of an arbitrary figure edge

value of between 1 and 2. A straight line has a fractal dimension of 1, while Brownian motion (Completely random movement) has a fractal dimension of 2. The fractal dimension for a highly irregular particle should have a value of approximately 1.4 (Flemmer et al., 1993).

The fractal dimension of a particle can be measured by 'walking' around the particle perimeter with a specified step length and measuring the subsequent perimeter length. The step length is then decreased and the 'walk' is repeated again. The procedure is repeated up to the smallest step length experimentally measurable. The results of this procedure is then plotted on a log-log graph where the perimeter length is plotted as a function of the step length. The fractal dimension can be obtained directly from this relationship.

The application of the different step sizes to measure the fractal dimension can be seen in figure A.3. This example gives an good indication that for small step sizes the particle perimeter is tracked relatively good, with most features included. At a much larger step size, only the general shape of the particle is tracked. Small features are completely ignored. As stated already the fractal dimension can be calculated directly from a log-log plot of the perimeter length as a function of the step length. An example of such a plot can be seen in figure A.4. The straight line relationship between the perimeter length and the step length around the particle can clearly be observed on the log-log plot. The specific particle investigated in figure A.4 has a fractal dimension of 1.012, which is an indication of a relatively smooth particle with little or no protrusions and indentations.

A.2.3 Polygonal harmonics

The human eye is very good at distinguishing different shapes. It is easy for us to say where a particle appears to be square, triangular or some other known shape, even though

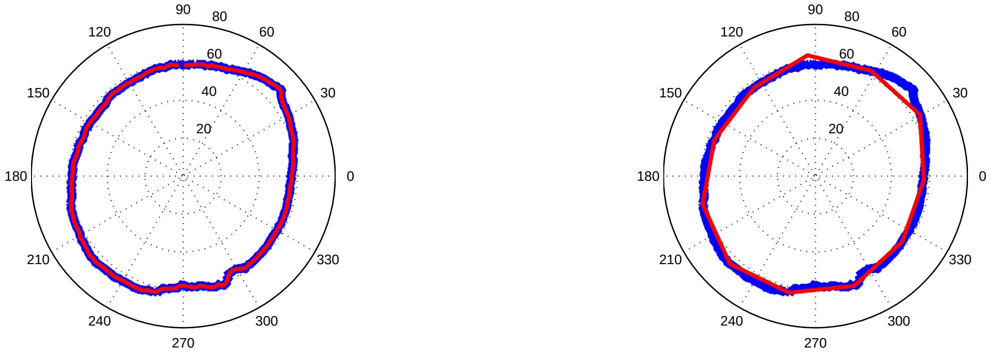

(a) Step length of 2.16 μm

(b) Step length of 34.5 μm

Figure A.3: An illustration of how the step size around the particle affects the perimeter length

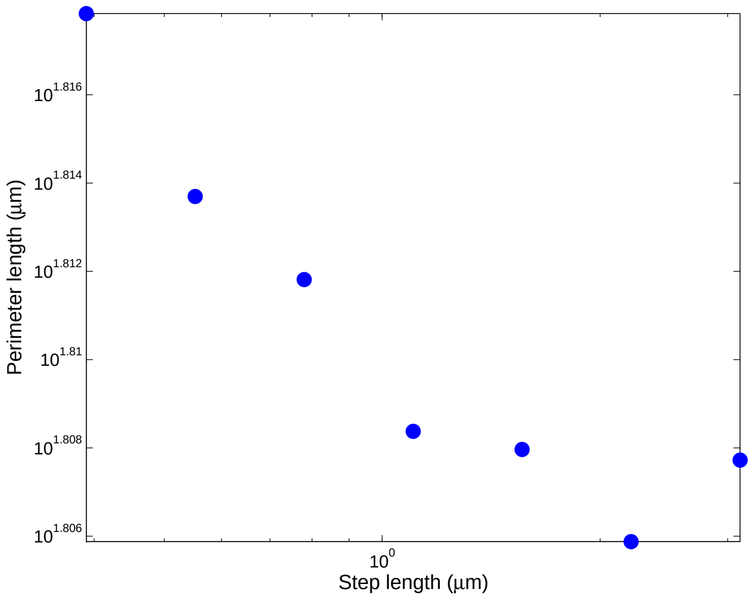

Figure A.4: A log-log plot used to calculate the fractal dimension the particle is not exactly that shape. In theory it should be relatively hard to develop a technique for an automated system, such as a computer, as computers are very exact. This would force the technique to have a very long list of rules that do not interfere with each other, which can be computationally intensive. One technique that gives a proper indication of the macro shape of a particle is to calculate the polygonal or fractal harmonic of a particle (Clark, 1987). The basis of polygonal harmonics are exactly the same as that of fractal dimensions. A specified step size is used to walk around a particle perimeter, however the process is not terminated once the perimeter has been circumvented but continues for a specified amount of circumventions. In almost all the cases the path walked will soon be repeated so that the walk will 'follow in its own footsteps'. This repeated walk or harmonic will form a regular polygon, where the steps taken will fall along the edges of the polygon. With different step lengths used, different polygons will be found. Normally the large step sizes are started with, therefore the first harmonic found will be the second harmonic, where two points on opposite sides of the particle edge are stepped between. The third harmonic will form a triangle inside the particle perimeter and the fourth harmonic a rhombus. This process can continue as far as the resolution of the particle edge allows for, but since polygonal harmonics are mostly used as a macro shape descriptor (Clark, 1987), the highest harmonic of real interest should be the fifth or sixth harmonic. An example of these harmonics can be seen in figure A.5. A specific harmonic for an object can exist, and usually do, for more than one step length. The range of step lengths for which a certain harmonic can be found is called the persistence of that harmonic and can be defined as shown in equation A.8.

(a) Simple third harmonic for a particle (b) Simple fourth harmonic for a particle

Figure A.5: Illustration of third and fourth harmonics for a particle

$$P_n = \frac{\mathrm{SL}_n\mathrm{max}}{\mathrm{SL}_n\mathrm{min}} \tag{A.8}$$

It has been found that the persistence of the third harmonic is high for triangular particles, while the persistence of the fourth harmonic is low for triangular particles (Clark, 1987). A list of harmonic persistences found for isometric can be seen in table A.1. Flemmer et al. (1993) found the third harmonic, P_3, to be a good shape descriptor to distinguish between different shapes in correlating fluidised bed hydrodynamics. Clark et al. (1989) used the second harmonic, P_2, to find a correlation between the drag coefficient and particle shape. It would therefore seem that there is no 'golden' harmonic to use for shape description, but one has to be found specific for a system. Polygonal harmonics are however very powerful to describe macro particle shapes.

Table A.1: Harmonic characteristics for isometric shapes (From Clark (1987))

Shape	Persistence of harmonic		
	2nd	3rd	4th
Perfect smooth circle	1	1	1
Equilateral triangle	1	2	1
Square	1.36	1	1.41
Scalene triangle	~1.5	~1.6	1

A.2.4 Piper's angle and Delta analysis

Cutbill (1971: p.97) as quoted by Flemmer et al. (1993) and Pickett et al. (1991) developed a technique to take a measure of the surface roughness of a particle. An illustration of how this technique works can be seen in figure A.6. This technique use an approximation of the particle silhouette with lines of equal length. These lines can be classified as leading and following vectors. The angle between the extension of the leading vector and the following vector can be measured for all of these lines. Note that a following vector become a leading vector if the next angle needs to be measured. A Piper's angle of 0° would therefore indicate a straight line. Note that the way Piper's angle is defined, the Piper's angle will always lie between 0° and 180°. A frequency plot of the angles between the lines are used to indicate the surface roughness of the particle. As a result of the constant step size used approximate the particle silhouette, the size of the steps will influence the features taken into account. Pickett et al. (1991) developed a new way to present the Piper's angles by plotting the average angle as a function of the step size. This method of representation allows one to see at which scale the particle is the most rugged and how rugged the particle is at this scale. A problem associated with Piper's

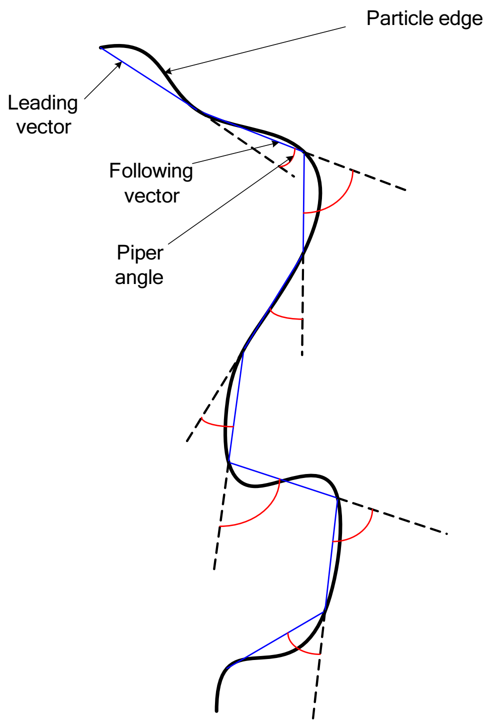

Figure A.6: Illustration of how Piper's angles are measured

angle is that two different features with a similar Piper's angle can have completely different hydrodynamic consequences. An example of this can be seen in figure A.7. In this example, the protruding feature marked by angle 2 and the receding feature marked by angle 1 have more or less the same Piper's angle, but these features will result in completely different hydrodynamic behaviour for a particle. A modification that can be used to correct for this short coming in the Piper's angle is to use the angle between the lines, either on the inside of the particle or on the outside of the particle. The inside of the particle refers to the angle between the lines closest to the centroid of the particle, where outside of the particle refers to the angle furthest from the centroid. When this modification is used, the Piper's angle will not lie between 0° and 180°, but between 0° and 360°.

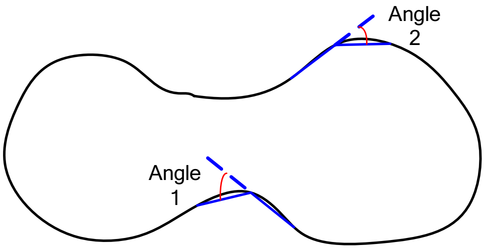

Figure A.7: An illustration of how Piper's angle can be lacking as a shape descriptor

A.2.5 Multi-scale roughness descriptor

All of the previously noted techniques either focus on the macro shape (Sphericity, Circularity and Polygonal harmonics), or micro structure (Heywood shape factor, Fourier coefficients, Fractal dimension and Piper's angles) of the particle under investigation. The problem associated with these techniques are that at least two descriptors are necessary to properly describe a particle shape. Drolon et al. (2000) developed a technique called the multi-scale roughness descriptor which is very useful for particle shape description. This technique utilise the harmonic wavelet transform (HWT) to classify the particle. By using the HWT as a classifier, it is possible to form a concept on all scales of what the particle looks like. The wavelet coefficients are calculated at different levels and these coefficients can then give an indication of the roughness at each of these levels. The lower levels give an indication of the macro shape of the particle, for example how elongated it is. Whereas the lower coefficients give an indication of how rough the surface of the particle is. The mathematics involved in the calculation of the multi-scale roughness descriptors are rather complex, and since this method will not be used in this study, the method will not be described in detail here. However, if interested, refer to Newland (1993) and Drolon et al. (2000) and Drolon et al. (2003).

APPENDIX B

Particle data extraction and manipulation

To process the shape information of the particles, the particle's shape will have to be available in a data set that can be processed mathematically. The simplest way to do this is to have the particle's perimeter represented as a data set of the distance from the centroid of the particle, r, and the swept angle from the starting position, θ. The starting position can be chosen arbitrarily. This data set will henceforth be referred to as the r-θ data. In figure B.1(a) an illustration can be seen of what is meant by r and θ.

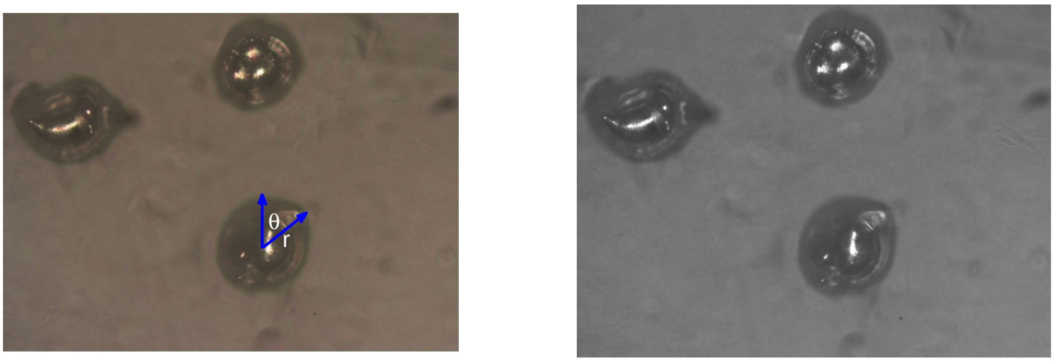

(a) Full colour image of the particles obtained from the microscope with r and θ indicated

(b) Example of grayscale image after manipulation of the full colour image

Figure B.1: Manipulation of image obtained from microscope from full colour image (a) to a greyscale image (b)

Note that both the light microscope and the SEM produces JPEG images. The process to extract the data from an image of either sources is therefore the same.

B.1 Image manipulation

JPEG images are full colour, high resolution photos, as can be seen in figure B.1(a). To be able to obtain the r-θ data with MATLAB, a black and white image is required. The black and white image can be obtained by thresholding a grayscale image, which in turn is found by processing the full colour image. These steps have to be done for each image taken of the particles.

B.1.1 Grayscale image

The grayscale image is a matrix where each cell in the matrix has a value of between 0 and 255, where 0 represents black and 255 represents white. The difference between the grayscale and the full colour image is that the full colour image has 3 matrices superimposed on each other. These matrices contain the intensity of the red, blue and green channels in the cells, with 0 being none of the specific colour and 255 being the full intensity of the specific colour.

To find a grayscale image that contains the most available information about the particles, the colour channel has to be chosen with the highest amount of sharp contours in intensity. This can mathematically be seen as the channel with the highest sum of derivatives.

The resultant grayscale image obtained from figure B.1(a) after choosing the best channel can be seen in figure B.1(b).

B.1.2 Black and White Image

The greyscale image in figure B.1(b) has two main features. These features are the background and the particles. Because of dirt on the microscope lens, rough features, etc, it is expected that noise will be present in both these features. This means that a Gaussian distribution of intensity can be expected for each feature. This bimodal Gaussian distribution can be seen in figure B.2. With this information known, the best value to threshold the grayscale image at, is the intensity level at which the two Gaussian distributions intersect.

With the threshold value for the image known, the black and white image can be displayed. Therefore all the cells in the matrix of the greyscale image with a intensity value below the threshold value will be displayed. This can be seen in figure B.3(a). However this figure still shows some noise and holes within the particles. Since it is known that all the particles are solid, these holes can be filled and the noise in the image can be cleaned. The resultant, cleaner image can be seen in figure B.3(b). The edge of the particle in a black and white image can be used to calculate the radius of the particle all along the edge, as well as the angle between the radius line and the radius

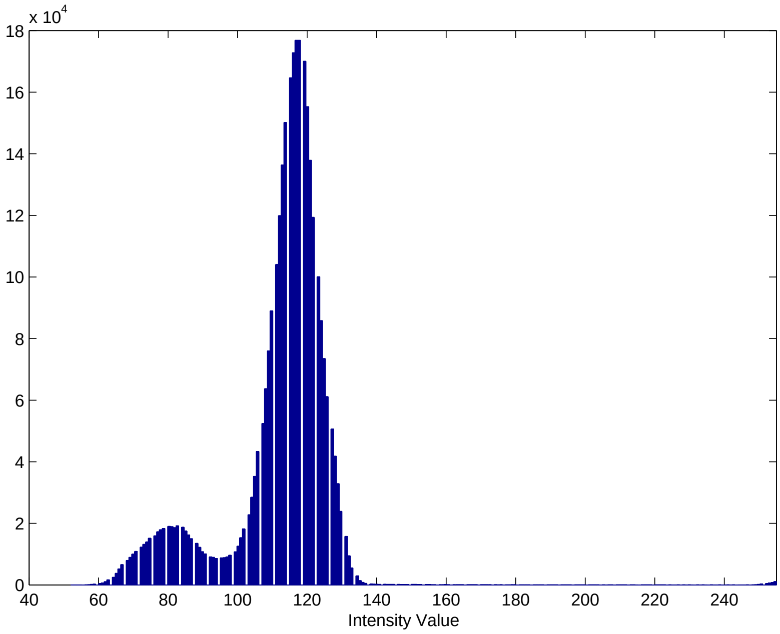

Figure B.2: Bimodal Gaussian distribution for the range of intensities in figure B.1(b)

(a) Black and white image obtained after thresholding the grayscale image in figure B.1(b)

(b) Cleaned black and white image ready for particle shape extraction

Figure B.3: Noisy black and white image (a) obtained after thresholding and cleaned black and white image (b) line of the starting position. A plot of one of the particles, in terms of the radius and the angle can be seen in figure B.4. This is the required r-θ data from which further shape characterisation is possible.

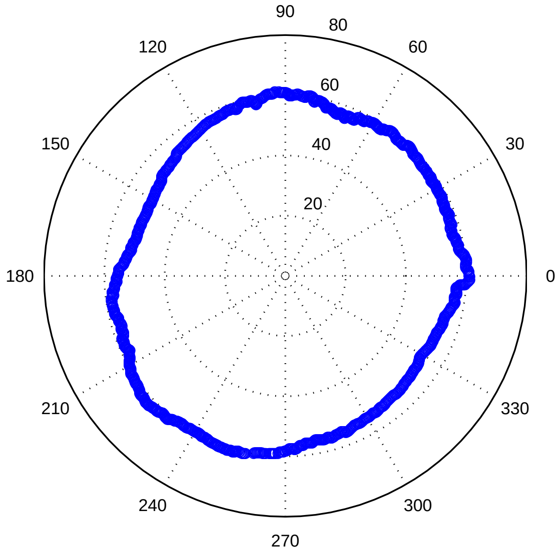

Figure B.4: Extracted particle border of one of the particles in figure B.3. Note that the dimension of the radius is μm

B.2 Particle shape characterisation

With the 2-dimensional data available for each of the particles, processing of the data can be done to characterise the shapes with the 2-dimensional shape characterisation methods discussed in appendix A. The sphericity of the particle cannot be properly calculated with 2-dimensional methods. However, the circularity can be calculated with ease by using equation 2.17 and can be used in the same way that the sphericity of a particle is used.

For all the modern shape classification techniques, it is necessary to approximate the particle edge with an array of lines that has the same length. The algorithm that approximates the edge starts off at a specified data point. The distance between the starting point and the next data point are then measured using the cosine rule in trigonometry. The distance is then compared with the specified step length (The length that each of the lines in the array of lines approximating the particle edge should have). If the distance between the data points are less than the specified step length, the distance between the starting point and the next data point is calculated. This process is continued until either the distance is exactly equal to the specified step length, or the distance exceeds the specified step length. In the case where the distance is equal to the specified step

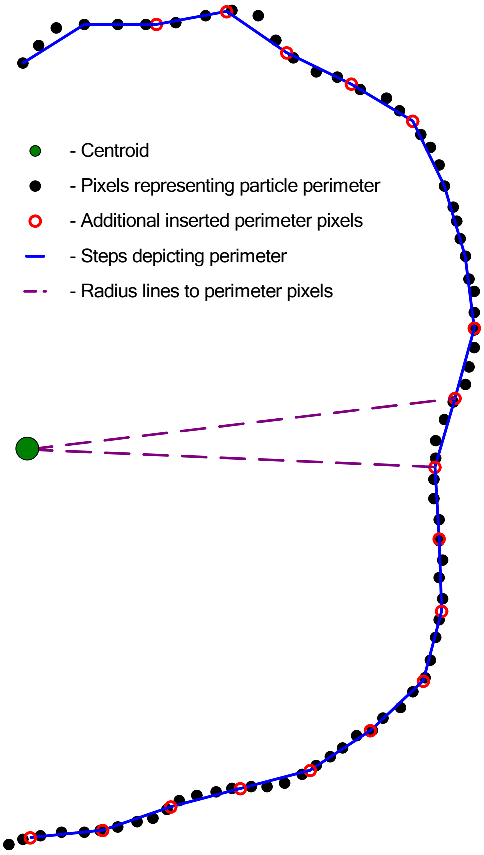

Figure B.5: A schematic illustration of how the particle perimeter is approximated with a series of lines of equal length

length, the data point to which this distance was measured is made the starting point and the process is repeated. However, if the distance exceeds the specified step length, a new data point is created by means of interpolation to which the distance is exactly the specified step length. This newly created data point is then made the starting point and the process is repeated. A schematic that shows this process graphically can be seen in figure B.5. This stepping around the particle perimeter is repeated until the particle perimeter is circumvented fully. The last line in the array are sometimes not of the same length as the other steps in the array, however, this is not a problem as the contribution of the last step to the total result is insignificant.

APPENDIX C

Particle shape analysis results

C.1 Modern techniques

C.1.1 Fractal dimension

The fractal dimension should, as stated in section A.2.2 give an indication on how rugged the surface of the particles are. To be able to use the fractal dimension to calculate the surface roughness of a particle, care have to be taken to ensure that the perimeter of the particle is in a sufficiently good enough resolution. The fractal dimensions for the mixtures can be seen in figure C.1. The results obtained in this figure is the opposite of what can be expected after looking at figure 3.5. It is expected that the fractal dimension of the milled FeSi should be much higher than that of the atomised FeSi. The explanation for this lack of compatibility with what one would expect is that the resolution of the images are simply just not high enough. To be able to quantify the roughness of a particle surface, the perimeter of one particle should fill the entire image. However, the time required to take a sufficient amount of images of individual particles on the SEM so that a statistically meaningful average is obtained is impractical. A further problem associated with the fractal dimension is that small artifacts on the perimeter of the particle can severely affect the calculated fractal dimension.

C.1.2 Piper's angle

Piper's angle is another technique that measures the surface roughness of a particle with the aid of image processing as described in section A.2.4. The Piper's angles are a function of the step size of the approximation of the particle edge. The same technique was used as described by Pickett et al. (1991), but instead of using the average Piper's angle for the batch of particles, the standard deviation of the Piper's angles for the batch

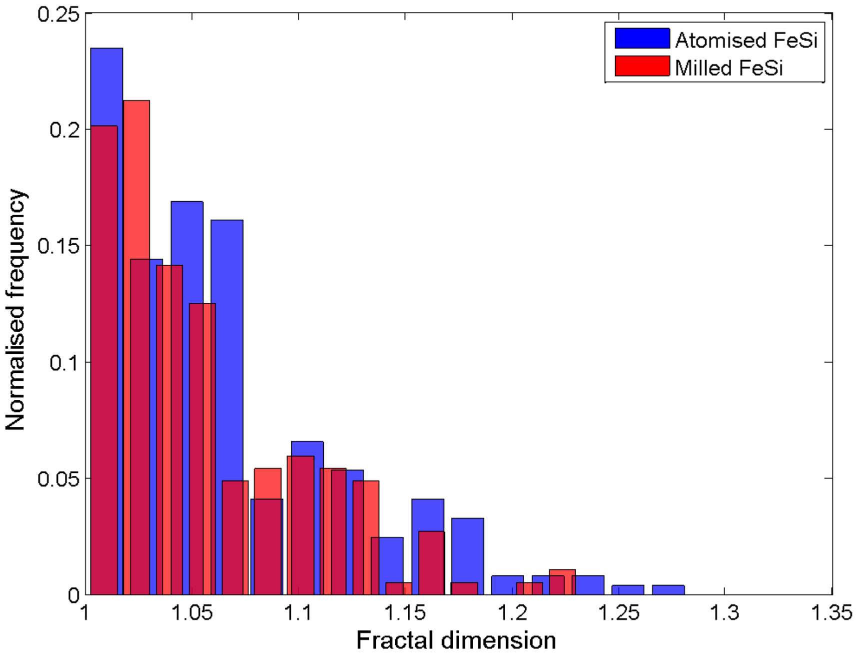

Figure C.1: The fractal dimensions for both the atomised and milled FeSi expressed in a frequency plot. $D_{f_{\text{avg}}}$ for milled FeSi = 1.056 and $D_{f_{\text{avg}}}$ for atomised FeSi = 1.065

of particles was used. The optimum step size was found to be $0.1\times d_{eq}$ of the particles. The frequency plot for the atomised and milled FeSi can be seen in figure C.2. As with the fractal dimension, the Piper's angle has severe inadequacies when trying differentiate between the atomised and milled FeSi. This is as a result of the resolution in the images of the particles. If a higher detail image can be taken of the particles, these techniques which measure particle shape based on micro structure of the particles can be used, however, with the available photos, the only techniques that should work properly to differentiate between the particles are those that measure macro shape.

C.1.3 Polygonal harmonics

Since all the shape description techniques which are based on the classification of the micro structure of the particle perimeter seems to be inefficient in differentiating between the two solid types, further investigation in shape description techniques which are based on the macro shape of the particle should be done. The persistence of polygonal harmonics has a good reputation for differentiating between different particle shapes. The results of the polygonal harmonics can be seen in figures C.3, C.4, C.5 and C.6.

The higher persistence of the second polygonal harmonic in the atomised particles is an indication that these particles are more elongated than the milled particles. This is in agreement with the process in which the atomised particles are made. The milled particles tend to be in their most stable position, which orientates the breadth and width

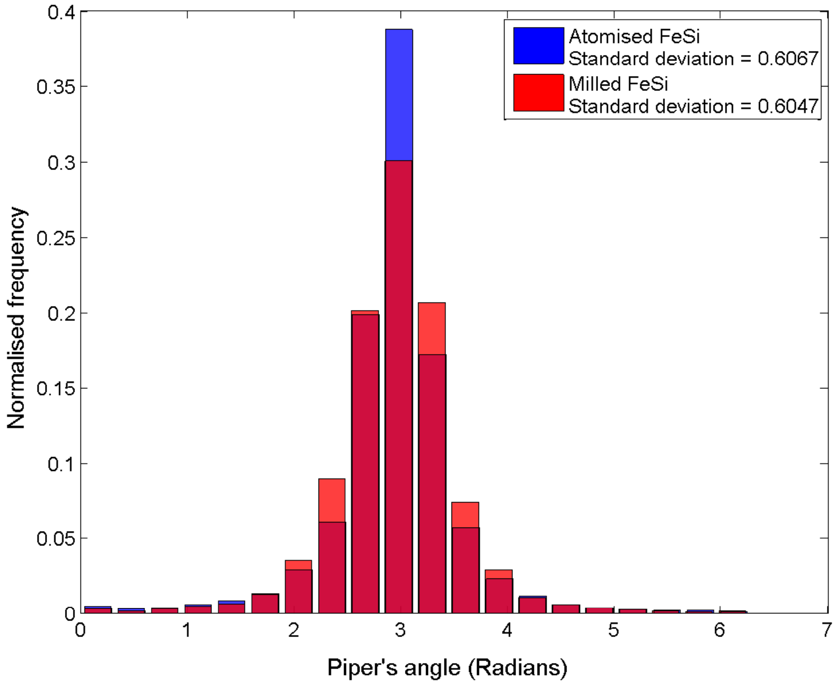

Figure C.2: Frequency plot of the Piper's angles for the atomised and milled FeSi batches

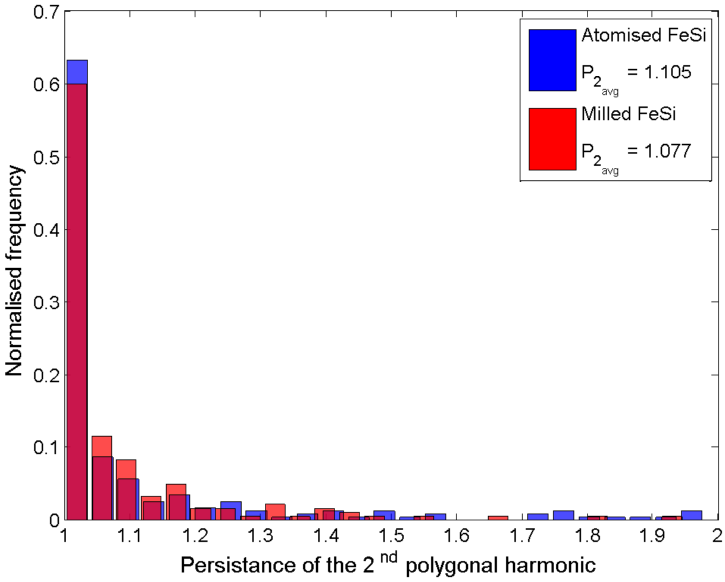

Figure C.3: Frequency plot of the persistence of the second polygonal harmonic

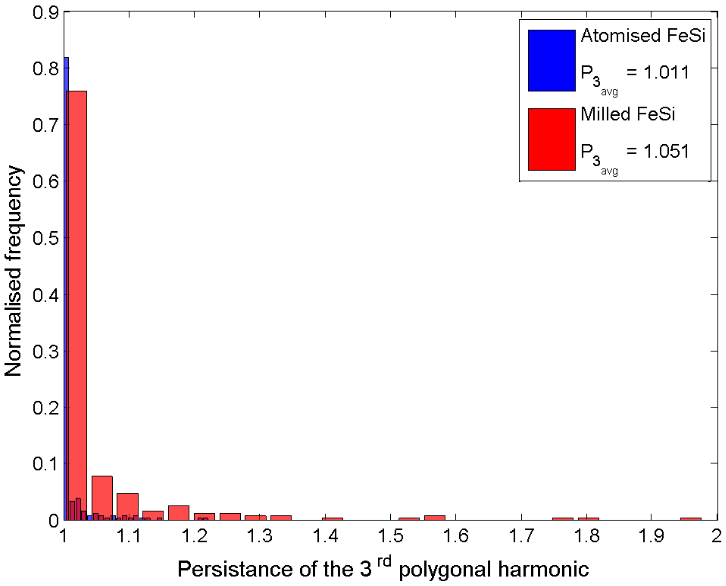

Figure C.4: Frequency plot of the persistence of the third polygonal harmonic

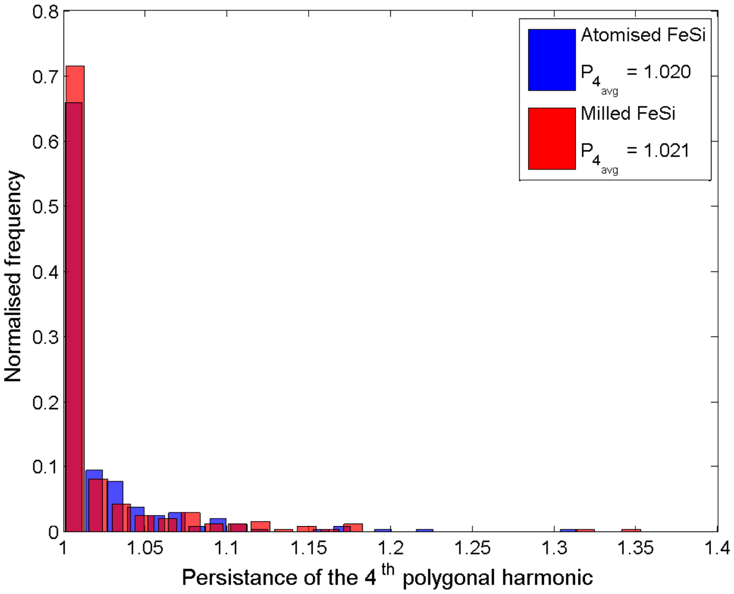

Figure C.5: Frequency plot of the persistence of the fourth polygonal harmonic

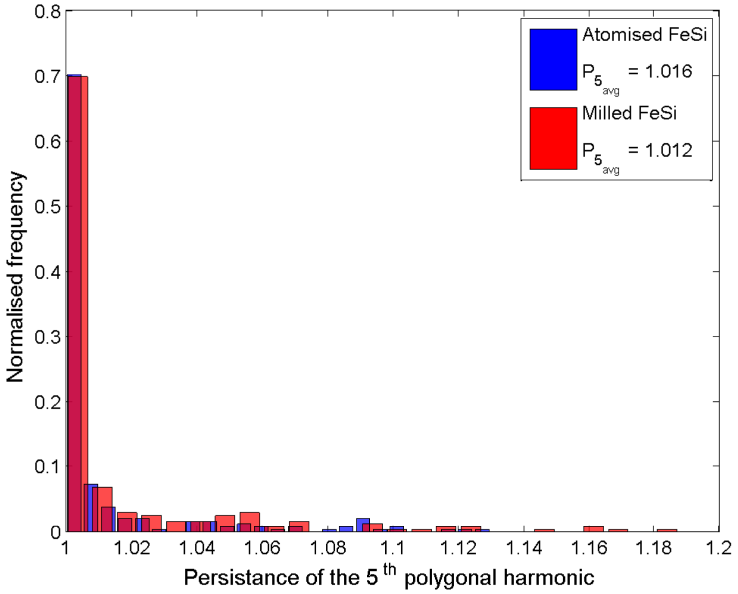

Figure C.6: Frequency plot of the persistence of the fifth polygonal harmonic

of the particles perpendicular to the direction of the electron beam from the SEM. This would explain why the milled particles have a low persistence for the second polygonal harmonic.

The third harmonic clearly indicates that the atomised particles have a mostly square shape, which would explain why persistence of the third harmonic is so low. The milled particles have a much wider distribution in the persistence of the polygonal harmonics, which indicates that a fair amount of triangularly shaped particles exists in the batch of particles.

The fourth harmonic confirms the square nature of the atomised particles, as seen with the third harmonic. This can also be explained by the method in which the atomised particles are produced, where the particles that do not separate into proper droplets form elongated globules so that they have rectangular shapes. The persistence for the milled particles are slightly higher, however, it is much lower than one would expect. With the plethora of irregular shapes found in the milled particles, it can only be expected that some are squarish, but the persistence of the fourth harmonic is much lower than that of the third harmonic. This means that the predominant shape among the milled particles are the slightly triangular ones.

The higher persistence in the fifth harmonic for the atomised particles can also be confirmed by the technique in which the atomised particles are formed. Even though the particles are mostly spherical in nature, quite a few of them get slightly elongated in the formation process.

The polygonal harmonics gives a good qualitative idea of how the morphology of the batches of particles differ, however, because such a large fraction of the particles have a persistence of 1 for most of the harmonics, it is not possible to get a quantitative idea of the particle shapes.